

# AirExo-2: Scaling up Generalizable Robotic Imitation Learning with Low-Cost Exoskeletons

Hongjie Fang<sup>\*,1</sup>, Chenxi Wang<sup>\*,2</sup>, Yiming Wang<sup>\*,1</sup>, Jingjing Chen<sup>\*,1</sup>,  
Shangning Xia<sup>1</sup>, Jun Lv<sup>1,2</sup>, Zihao He<sup>1</sup>, Xiyan Yi<sup>1</sup>, Yunhan Guo<sup>1</sup>, Xinyu Zhan<sup>1</sup>,  
Lixin Yang<sup>1</sup>, Weiming Wang<sup>1</sup>, Cewu Lu<sup>†,1</sup> and Hao-Shu Fang<sup>†,1</sup>

**Abstract**—Scaling up imitation learning for real-world applications requires efficient and cost-effective demonstration collection methods. Current teleoperation approaches, though effective, are expensive and inefficient due to the dependency on physical robot platforms. Alternative data sources like in-the-wild demonstrations can eliminate the need for physical robots and offer more scalable solutions. However, existing in-the-wild data collection devices have limitations: handheld devices offer restricted in-hand camera observation, while whole-body devices often require fine-tuning with robot data due to action inaccuracies. In this paper, we propose *AirExo-2*, a low-cost exoskeleton system for large-scale in-the-wild demonstration collection. By introducing the demonstration adaptor to transform the collected in-the-wild demonstrations into pseudo-robot demonstrations, our system addresses key challenges in utilizing in-the-wild demonstrations for downstream imitation learning in real-world environments. Additionally, we present *RISE-2*, a generalizable policy that integrates 2D and 3D perceptions, outperforming previous imitation learning policies in both in-domain and out-of-domain tasks, even with limited demonstrations. By leveraging in-the-wild demonstrations collected and transformed by the *AirExo-2* system, without the need for additional robot demonstrations, *RISE-2* achieves comparable or superior performance to policies trained with teleoperated data, highlighting the potential of *AirExo-2* for scalable and generalizable imitation learning. Project page: <https://airexo.tech/airexo2>.

## I. INTRODUCTION

Scaling up generalizable robotic imitation learning in the real world is essential for developing robust policies that can be directly applied to practical scenarios [3, 6]. While teleoperation has been commonly used to collect demonstrations for imitation learning, it requires a physical robot platform to record both observations and robot actions, raising costs due to the expensive hardware involved. Despite its effectiveness, this approach is costly and inefficient for scaling up demonstration collection for imitation learning.

Recently, researchers have explored several alternative data sources that can be scaled up at a lower cost, such as human videos [4, 85, 91, 94, 102, 106] and in-the-wild demonstrations [26, 18, 83, 93, 109]. Unlike traditional robot-centric demonstrations collected through teleoperation, both sources focus on human-centric demonstrations. This eliminates the need for a physical robot during data collection,

greatly reducing costs and enhancing scalability. For human videos, actions are typically inferred using hand detection and pose estimation [71, 91], or inferred from object pose during interactions [32, 107]. In contrast, in-the-wild demonstrations utilize additional devices to interface humans and robots, capturing the observation and action data relevant to robotic manipulations when the human is performing the task.

Current devices for collecting in-the-wild demonstrations can be broadly categorized into two classes: handheld devices [18, 22, 82, 83, 109] and whole-body devices [26, 15, 50]. Handheld devices are typically designed with end-effectors identical to those of the robot. By equipping both the handheld devices and the robot with in-hand cameras, these methods leverage in-hand observations to ensure visual consistency. However, they have two main limitations: (1) the pose estimation of the devices often relies on visual SLAM algorithms, which can introduce inaccuracies in capturing actions (§VI-B), and (2) the in-hand camera has a limited field of view and struggles to capture accurate depth information during interactions between the robot and objects (§V-B). On the contrary, whole-body devices are usually more accurate in action capturing and offer flexible observation options. However, they generally use in-the-wild demonstrations for pre-training and require additional teleoperation data to fine-tune the policy. The underlying reason for this limitation is that *the data from in-the-wild demonstrations still exhibits a domain gap compared to the data from the real robot*.

To address these challenges, we introduce the *AirExo-2* system for large-scale in-the-wild demonstration collection and adaptation. As shown at the top of Fig. 1, we propose a demonstration adaptor to transform the in-the-wild demonstrations into pseudo-robot demonstrations, both observations and actions from the in-the-wild demonstrations can be effectively aligned with the robot domain. This transformation enables the demonstrations to be directly applicable to downstream imitation learning policies. From the hardware perspective, we develop an updated exoskeleton built upon AirExo [26], tailored for easy demonstration adaptation process. It provides a stronger mechanical structure and more accurate calibration, making the action capturing more precise and the system more robust. Comprehensive analyses are conducted to evaluate the efficiency and accuracy of the *AirExo-2* system in collecting demonstrations.

Beyond scaling up in-the-wild demonstration collection, developing a robust policy is crucial for effectively utilizing

\* These authors contributed equally. E-mails: galaxies@sjtu.edu.cn, cxwang85@gmail.com, sommerfeld@sjtu.edu.cn, jjchen20@sjtu.edu.cn

<sup>1</sup> Shanghai Jiao Tong University.

<sup>2</sup> Shanghai Noematrix Intelligence Technology Ltd.

<sup>†</sup> Cewu Lu and Hao-Shu Fang are the corresponding authors. E-mails: lucewu@sjtu.edu.cn, fhaoshu@gmail.com



**Fig. 1: Overview of the *AirExo-2* System and the *RISE-2* Policy.** (Top) The *AirExo-2* system enables the scalable collection and effective adaptation of in-the-wild demonstration data. A demonstration adaptor is employed to convert in-the-wild demonstrations into pseudo-robot demonstrations that are directly usable for training imitation learning policies. (Bottom) The proposed generalizable policy, *RISE-2*, can effectively leverage these converted pseudo-robot demonstrations for learning manipulation skills, enabling zero-shot deployment on real-world dual-arm robots without requiring any teleoperated demonstrations, and achieving results comparable to policies trained with the same amount of teleoperated data.

these demonstrations. To this end, we introduce *RISE-2*, a generalizable policy that seamlessly integrates both 2D and 3D perceptions, as shown at the bottom of Fig. 1. Experiments show that *RISE-2* not only outperforms previous imitation learning policies in in-domain evaluations, but also surpasses prior generalizable policies in several out-of-domain scenarios, even when trained on a limited number of demonstrations from a narrow domain. Leveraging the strong generalization capabilities of *RISE-2*, we show that using in-the-wild demonstrations collected and adapted by the *AirExo-2* system, *without requiring additional demonstrations from the robot domain*, our policy achieves results comparable to, or even exceeding, those of imitation policies trained on an equivalent amount of teleoperated data.

## II. RELATED WORKS

### A. Scaling up Demonstration Collection

Demonstration data is essential for advancing imitation learning in robotic manipulation, as it serves as a foundation for learning complex and structured behaviors from expert demonstrations. Recent research on data scaling laws [56] has

revealed that similar scaling patterns emerge in imitation learning for robotic manipulation, analogous to those previously identified in natural language processing [46] and computer vision [31, 72] fields. This highlights the importance of scaling up the demonstration collection.

Currently, there are four main directions for acquiring demonstration: teleoperation, generation in simulation, human video, and in-the-wild data collection.

**Teleoperation.** A straightforward method for collecting real-world robot demonstrations is human teleoperation, which directly captures demonstrations in the robot domain and is widely regarded as one of the most effective data collection techniques in real-world robotic imitation learning. However, it presents several challenges, especially when it comes to scalability. Scaling up teleoperated-based demonstration collection requires increasing the number of both robots and teleoperation devices, with robots being particularly costly to scale. Therefore, current large-scale robotic manipulation datasets collected through teleoperation [8, 20, 25, 42, 49, 92, 104] usually require significant human and physical resources in the data collection process. Another drawback is inefficiency, as

teleoperating robots to complete tasks is far less intuitive than performing the tasks directly with human hands, leading to high learning costs [60] and suboptimal demonstrations [11].

**Generation in Simulation.** This line of research addresses the demonstration scaling problem by automatically generating or augmenting demonstrations in simulation. Several studies generate demonstrations with large language models and skill-level agents [40, 67, 99, 101], while other approaches augment few human teleoperated demonstrations through replay [1, 37, 45, 65, 97]. Although these methods simplify the demonstration generation process, policies trained on such demonstrations often require additional sim-to-real adaptation before they can be applied in real-world scenarios.

**Human Video.** Researchers have also explored leveraging internet-scale human videos for robotic manipulation policy learning. Some approaches [2, 62, 63, 64, 68, 77, 87, 111] focus on visual representation learning from human videos, while others [4, 10, 29, 75, 103, 108] propose pre-training the policy backbone with auxiliary video or latent prediction objectives. Since accurately extracting human hand states and 3D spatial trajectories from 2D videos remains challenging [66], it is still difficult to convert human videos into usable demonstrations for direct training the policies without fine-tuning on additional in-domain robot demonstrations.

**In-the-Wild Data Collection.** In-the-wild data refers to demonstrations collected by humans using specialized hardware devices, such as hand-held grippers [18, 22, 82, 83, 109], hand-held cameras [21, 98], VR/AR glasses [15, 47, 50], motion-capture gloves [93], and exoskeletons [26, 50]. These devices act as a bridge between humans and robots, translating human hand motions into corresponding robot end-effector actions during demonstration collection. Without the dependency of physical robots, it is cost-effective for collecting in-the-wild demonstrations at scale. Nonetheless, challenges remain in improving the accuracy of such motion translation and addressing visual inconsistencies between humans and robots.

### B. Learning from In-the-Wild Demonstrations

Despite promising in terms of scalability, two domain gaps pose obstacles in learning from in-the-wild demonstrations: the kinematic gap and the visual gap [26, 50]. The kinematic gap refers to the discrepancy in motion translation between humans and robots, where inaccuracies can affect action quality to some extent. The visual gap, on the other hand, pertains to the fact that visual information captured in in-the-wild demonstrations often includes specialized devices and human hands, whereas the visual information in robot demonstrations and deployments should contain the robot itself.

**Kinematic Gap.** The kinematic gap can be bridged using either visual or mechanical methods. DemoAT [109] employs structure-from-motion [81] to approximate the end-effector pose from a sequence of RGB images. Other visual methods leverage off-the-shelf pose estimation frameworks from commercial cameras, such as GoPro [18], iPhone Pro [21, 22, 83, 98], RealSense T265 [15, 82, 93], and Aria glasses [47].

Mechanical methods typically build isomorphic devices [26, 50] that obtain the robot poses from angle encoder readings.

**Visual Gap.** Hand-held devices [18, 22, 82, 83, 109] rely solely on in-hand cameras for visual observation and employ the same end-effector during robot deployment to prevent visual inconsistencies. Most other methods address the visual gap by incorporating additional real robot demonstration data for fine-tuning or co-training [21, 26, 47, 98], or by using human-in-the-loop techniques to collect corrective behaviors during policy deployment [15, 93]. M2R [50] utilizes cropped observations with limited fields of view to reduce the impact of visual inconsistencies.

### C. Generalizable Manipulation Policy

Direct learning from in-the-wild demonstrations emphasizes the need for a generalizable manipulation policy. Such a policy must effectively transfer the skills learned from in-the-wild demonstrations to the robot during real-world deployment. A generalizable policy is defined by its ability to adapt to new domains or environments, even when trained with limited demonstrations from a restricted domain [105]. Specifically, it should be capable of generalizing across variations such as different camera perspectives, backgrounds, objects, and even embodiments.

Although many behavior-cloning-based [73] robotic manipulation policies [17, 27, 28, 84, 116] have demonstrated strong performance during in-domain evaluations, they often struggle in out-of-distribution scenarios, leading to compounded errors and task failures [96, 105]. While large-scale pre-training on real-world robot demonstration data can improve the generalization ability of a robotic manipulation policy to some extent [5, 8, 20, 42, 52, 58, 69, 100, 120], it does not overcome the inherent upper bound of the policy’s generalization ability, *i.e.*, its fundamental capacity to adapt across diverse domains and contexts in manipulation tasks.

Leveraging 3D perceptions [14, 27, 28, 96, 110] and 2D foundation models [9, 57, 74, 105, 112] are two promising avenues towards generalizable manipulation policies. The former utilizes geometric cues to supplement the policy’s understanding of the physical environment, while the latter harnesses the rich semantic features of 2D foundation models [16, 54, 70, 76, 79] to improve the policy’s ability to recognize and interpret complex object and scene information. Recent studies [44, 114, 115] have explored combining these two approaches to further enhance policy performance. However, challenges remain in effectively integrating these insights for better generalization across diverse manipulation domains.

## III. AIREXO-2: COLLECTING AND ADAPTING IN-THE-WILD DEMONSTRATIONS

### A. Overview

*AirExo-2* prioritizes in-the-wild demonstration collection and subsequent data adaptation. Our goal is to *efficiently collect and adapt in-the-wild demonstrations into pseudo-robot demonstration for direct use in training real-world robotic manipulation policies*, which is particularly suitable

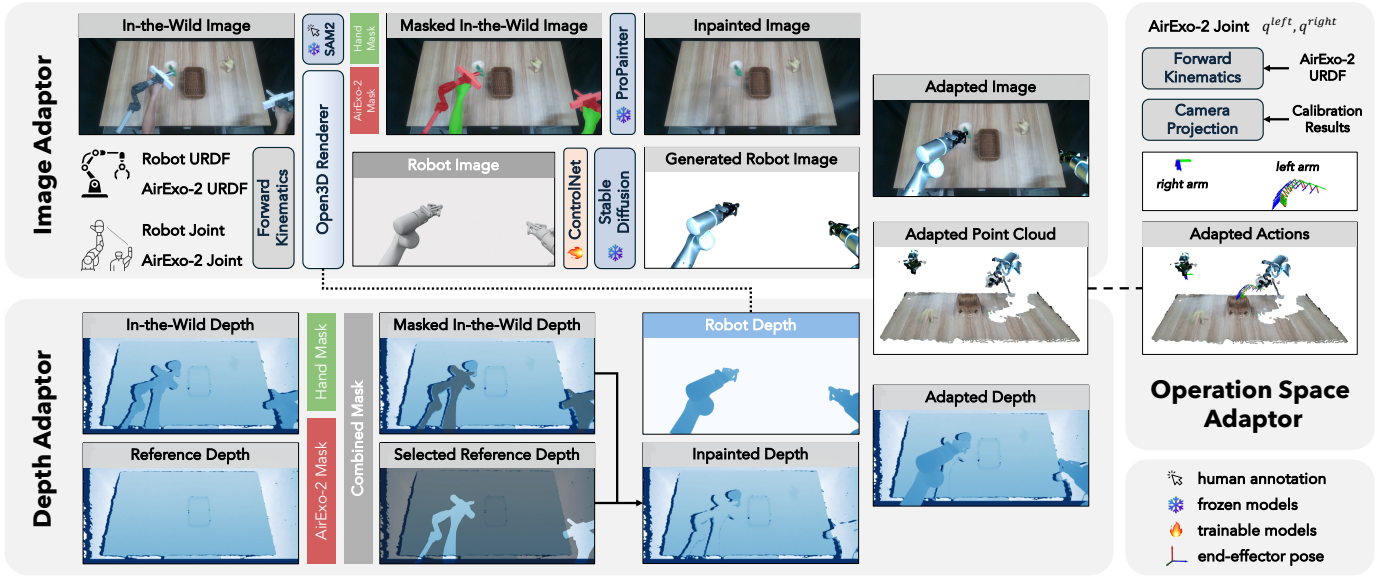


**Fig. 2: Illustration of the Demonstration Adaptor.** We propose a demonstration adaptor to convert in-the-wild demonstrations into pseudo-robot demonstrations. It comprises three modules: an **operation space adaptor** for kinematic transformation, an **image adaptor** for visual processing, and a **depth adaptor** for depth adaptation.

for scaling up demonstration collection at a low cost. From this perspective, the main issues that need to be solved are:

- D1.** The operation space from the in-the-wild demonstrations should be aligned with those of the robot, bridging the kinematic gap.
- D2.** The visual observations from both in-the-wild demonstrations and robot deployment should be transformed into a unified domain, addressing the visual gap.

These two issues require a robust hardware and accurate calibration process to ensure the action capturing aligns well with the robot space, therefore facilitating subsequent demonstration adaptation. We detail the updated exoskeleton hardware design and calibration process in Appendix A and Appendix B, respectively. The whole system retains the low-cost advantage of AirExo [26], with the dual-arm demonstration collection platform (excluding the camera) priced at only \$600. All hardware models, data collection code, and installation guides will be open-sourced. The demonstration adaptation process is introduced as follows.

### B. Demonstration Adaptor

As discussed in §II-B, in-the-wild demonstrations often exhibit significant visual and kinematic differences from robot demonstrations, hindering their direct use for robotic manipulation policy learning. Prior approaches typically *avoid* the visual gap by using in-hand cameras or relying on pre-training and fine-tuning. In contrast, our *AirExo-2* system *solves* the visual gap by employing adaptors to convert in-the-wild observations into pseudo-robot observations. Together with an operation space adaptor that unifies the coordinate system of both demonstrations into the camera coordinates, these components form the demonstration adaptor. The demonstration adaptor helps align the in-the-wild data more closely with the robot’s operating conditions, enabling the learned policies to be more

*directly transferable* to real-world robotic manipulation tasks. Fig. 2 shows an overview of our demonstration adaptor.

**Operation Space Adaptor (D1).** Theoretically, we can transform the end-effector poses of both arms into the device base for both *AirExo-2* and the dual-arm robot platform, as they are morphologically identical. However, achieving such precision during the installation of the robotic arms is challenging, which means that we need to treat the dual-arm robot system as two separate single-arm robot systems in practice. This results in the device base not being a universal coordinate frame. Therefore, we opt to project all states and actions into the global camera coordinate system using the calibration results.

**Image Adaptor (D2).** With the recorded *AirExo-2* encoder readings and the calibrated transformation between the global camera and the *AirExo-2* base, we integrate the *AirExo-2* model into the Open3D rendering engine [117]. Using similar methods as previously described in the calibration section, we can render RGB-D and mask images of *AirExo-2*. Due to the one-to-one joint mapping between *AirExo-2* and the dual-arm robot, we can also render the corresponding RGB-D and mask images of the dual-arm robot.

In addition to obtaining the *AirExo-2* mask from the renderer, we also need to address the visual information related to the human hands in the in-the-wild demonstrations. To achieve this, we use SAM-2 [78] to generate a consistent hand mask throughout the demonstration video. By merging this mask with the *AirExo-2* mask, we can identify the regions where the in-the-wild demonstration visually differs from the robot demonstration. Next, we apply the pre-trained video inpainting model ProPainter [118] to fill in the masked areas, effectively removing the human embodiment information from the images to generate agent-agnostic images. Inspired by [12], we then fine-tune a pre-trained Stable Diffusion 1.5 [79] model with

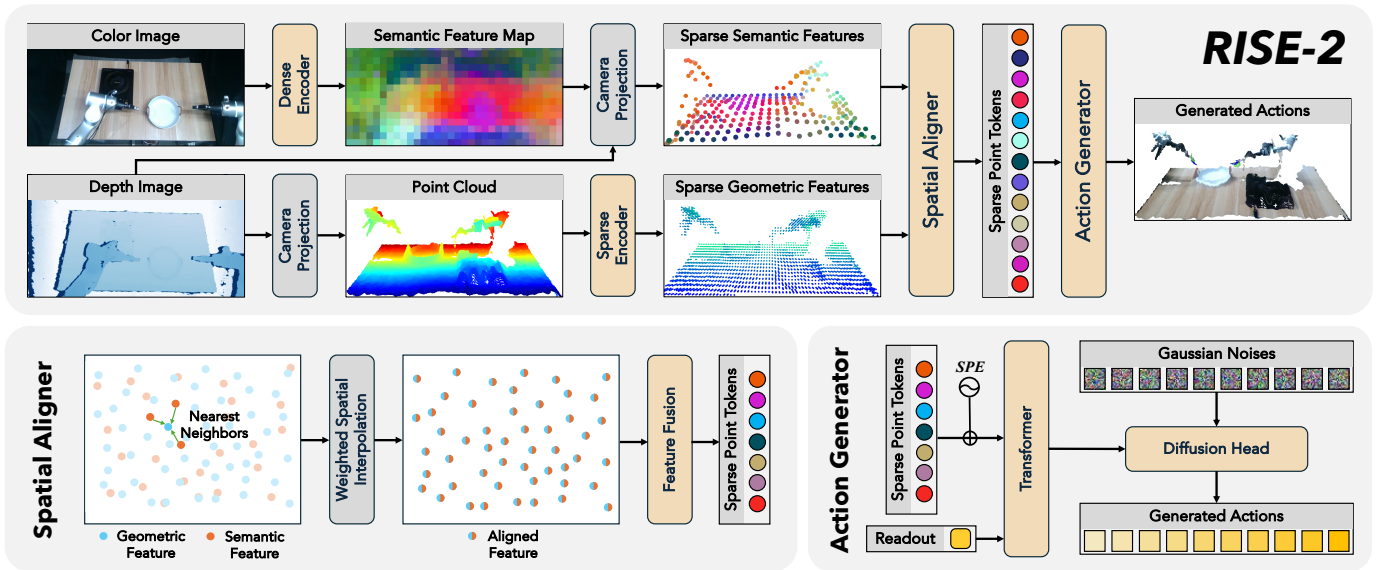


**Fig. 3: *RISE-2* Policy Architecture.** *RISE-2* takes an RGB-D observation as input and generates continuous actions in the camera frame. It is composed of four modules: 1) the color image is fed into the **dense encoder** to obtain semantic features organized in 2D form, which is then projected to sparse 3D form using reference coordinates; 2) the depth image is transformed to a point cloud and fed into the **sparse encoder** to obtain the local geometric features of seed points; 3) in the **spatial aligner**, the semantic features and the geometric features are aligned and fused using their 3D coordinates; 4) in the **action generator**, the fused features are converted to sparse point tokens, mapped to action space using a transformer and sparse positional encoding (*SPE*), and decoded into continuous actions by a diffusion head.

ControlNet [113] to generate photorealistic robot images from the rendered robot images. These generated robot images are then extracted using the robot mask and superimposed onto the inpainted images, producing the final pseudo-robot images.

**Depth Adaptor (D2).** For depth adaptation, we first capture a reference depth image of the empty workspace using the same camera setup, serving as a universal background reference. For each task, we identify static objects in the scene and record their depth values in the first frame as a demonstration-specific background reference. Using the merged mask provided by the image adaptor, we determine the regions of the depth map requiring adaptation and replace them with corresponding values from the demonstration-specific background. This process effectively removes depth information associated with human embodiment while preserving the scene’s spatial consistency. Finally, by integrating the inpainted depth with the rendered robot depth, we can obtain the adapted depth.

#### IV. *RISE-2*: A GENERALIZABLE POLICY FOR LEARNING FROM IN-THE-WILD DEMONSTRATIONS

##### A. Overview

Although we have transformed in-the-wild demonstrations into pseudo-robot demonstrations, inherent domain gaps such as differences in camera perspectives remain. Therefore, a generalizable policy is crucial for efficiently and effectively learning from these transformed in-the-wild demonstrations produced by the *AirExo-2* system.

As discussed in §II-C, 3D perception and 2D foundation models play complementary roles in creating a generalizable policy. 3D perception captures view-invariant geometric features of the scene, while 2D foundation models utilize their

extensive knowledge to extract rich semantic features. Notably, 3D perception is especially beneficial for learning from in-the-wild demonstrations, as it explicitly infers spatial positions using a single camera, unlike 2D policies that often rely on multiple cameras to determine positions indirectly.

Building on these insights, we propose a 3D generalizable policy, *RISE-2*, to facilitate efficient learning from in-the-wild demonstrations and achieve robust task performance. Built upon RISE [96], our *RISE-2* policy addresses the following limitations of the original approach:

- P1.** The raw point and color information are jointly encoded in RISE, causing geometric and semantic features to interfere with each other, which leads to consistent positional offsets in output actions when the background changes.
- P2.** The inevitable noise in depth sensors often results in low-quality point cloud textures, making it challenging to extract rich semantic features solely from point cloud data and limiting the model’s scene understanding capabilities.
- P3.** The sparse encoder lacks pretraining on large-scale 3D scene datasets, hindering its ability to generalize across varying instances, backgrounds, and embodiments. Moreover, large-scale pretraining for 3D data introduces significant computational overhead, which is impractical for a shallow encoder.

Based on the above limitations, the design of *RISE-2* focuses on the precise feature fusion of 2D images and 3D point clouds to leverage the advantages of 2D vision in semantic information and 3D vision in spatial information simultaneously.

## B. Policy Architecture

As shown in Fig. 3, *RISE-2* consists of four modules: a **sparse encoder** for 3D geometric feature extraction, a **dense encoder** for 2D semantic feature extraction, a **spatial aligner** for 2D-3D feature fusion and an **action generator** to decode visual features into actions. The implementation details are listed in Appendix E.

**Sparse Encoder (P1).** 3D point cloud data contains rich spatial structure information, which greatly facilitates the extraction of local geometric features. Such property has been successfully applied in general grasping [23, 24, 95]. RISE featurizes the point cloud data with raw color information to obtain the semantic cues and geometric cues simultaneously, but fails to distinguish the coordinate shift and the color shift. *RISE-2* inherits the sparse 3D encoder [19] from RISE, but removes the color information to obtain pure geometric features. We denote this module by  $E_s$ , which implements the transformation from depth image to sparse geometric features:

$$E_s : (\mathbf{D}, K) \rightarrow (\mathbf{F}_g, \mathbf{C}_g), \quad (1)$$

where  $\mathbf{D}$  denotes the observed depth image,  $K$  denotes the corresponding camera intrinsic, and  $\mathbf{C}_g = \{c_i^g \in \mathbf{P}\}$  denotes the seed points after network down-sampling.  $\mathbf{D}$  is firstly converted to a point cloud  $\mathbf{P}$  using camera intrinsic  $K$ . The sparse network takes  $\mathbf{P}$  as input and extracts the local geometric features  $\mathbf{F}_g = \{f_i^g\}$ , where  $f_i^g$  is the corresponding feature vector of  $c_i^g$ . This lightweight encoder enhances the efficiency of sparse feature extraction, ensuring the real-time performance of the policy.

**Dense Encoder (P2 and P3).** A generalizable policy requires rich semantic features to understand the scene, while the low-quality texture of point cloud data poses a challenge to this demand. Unlike RISE, *RISE-2* adopts a dense 2D encoder to process organized color information, which is denoted by  $E_d$ .  $E_d$  implements the transformation from color image to dense semantic features:

$$E_d : (\mathbf{I}, \mathbf{D}, K) \rightarrow (\mathbf{F}_s, \mathbf{C}_s), \quad (2)$$

where  $\mathbf{I}$  denotes the observed color image and  $\mathbf{F}_s = \{f_i^s\}$  denotes the output semantic feature map with the width  $w$  and the height  $h$ . Since  $\mathbf{F}_s$  is densely organized in 2D form, we also compute its reference 3D coordinates  $\mathbf{C}_s = \{c_i^s\}$  for the mapping to sparse form. Let the raw point cloud  $\mathbf{P}$  be organized in 2D form,  $\mathbf{C}_s$  is computed by:

$$\mathbf{C}_s = \text{AdaptiveAvgPool2d}(\mathbf{P}, [w, h]), \quad (3)$$

where  $\text{AdaptiveAvgPool2d}(\cdot, [w, h])$  applies an average pooling function to  $\mathbf{P}$ , and the output shape is  $w \times h$ . By leveraging continuous color information distributed in high-resolution data,  $E_d$  significantly enhances the policy’s ability to capture the details in the scene.

One significant advantage of the dense encoder is the usage of visual foundation models, offering highly generalized visual representations that excel across diverse tasks and domains [105]. *RISE-2* employs DINOv2 [70] fine-tuned with

LoRA [39] to implement  $E_d$ . Such design improves the policy’s robustness and adaptability in understanding contextual relationships within the environments.

**Spatial Aligner (P1).** *RISE-2* extracts the geometric features and the semantic features using separate encoders, posing a challenge for the fusion of features distributed in different domains. One solution is to directly concatenate the two aggregated feature vectors, but it loses fine-grained local features which are vital for precise perception. Another alternative upsamples  $\mathbf{F}_s$  to the size of the original dense image  $\mathbf{I}$ , projects it to the point cloud  $\mathbf{P}$ , and downsamples the features to align with the seed points  $\mathbf{C}_g$  [114]. This approach incurs a high computational cost, decreasing the efficiency of policy training and deployment.

Instead, *RISE-2* utilizes a spatial aligner to efficiently fuse the two kinds of features based on their 3D coordinates  $\mathbf{C}_g$  and  $\mathbf{C}_s$ . For a point  $c_i^g \in \mathbf{C}_g$  output by the sparse encoder  $E_s$ , we compute its nearest neighbors  $\mathbf{N}_i = \{n_j^s | j = 1, \dots, M\}$  from  $\mathbf{C}_s$  output by the dense encoder  $E_d$ . The semantic feature of  $c_i^g$  is computed by weighted spatial interpolation:

$$f_i^* = \frac{\sum_{j=1}^M f_j^s / \text{dist}(c_i^g, n_j^s)}{\sum_{j=1}^M 1 / \text{dist}(c_i^g, n_j^s)}, \quad (4)$$

where  $\text{dist}(c_i, c_j)$  is the Euclidean distance between  $c_i$  and  $c_j$ . The aligned feature of point  $c_i^g$  is

$$f_i = \text{Concat}(f_i^g, f_i^*). \quad (5)$$

By aligning the seed points  $\mathbf{C}_g$  with the dense feature map  $\mathbf{F}_s$  using 3D coordinates, we can easily obtain the precise semantic features of points in different locations. The aligned features are then fused to high-level sparse representations using sparse convolution layers [19]. The visualization results of applying weighted spatial interpolation to the 2D feature map can be found in Appendix H.

**Action Generator.** The action generator adopts a similar architecture to RISE, which uses a transformer [90] to approximate the mapping from point features with sparse positional encoding to the action space, and a diffusion head [17, 33, 43] to generate the action chunk [116]. The transformer in *RISE-2* is in a decoder-only form, taking sparse point tokens and a readout token as input. Conditioning on the feature of the readout token, the diffusion head decodes the Gaussian noises into continuous actions. The generated actions are in the camera frame to ensure consistency across different scenes and camera views. The translations are in absolute positions and the rotations are in 6D representation [119].

## V. EXPERIMENTS

In this section, we aim to answer the following research problems.

- Q1. Are in-hand cameras sufficient for effectively perceiving and executing manipulation tasks?
- Q2. Does *RISE-2* outperform previous policies in in-domain evaluations?
- Q3. Can *RISE-2* generalize to environmental disturbances, such as unseen objects and backgrounds?

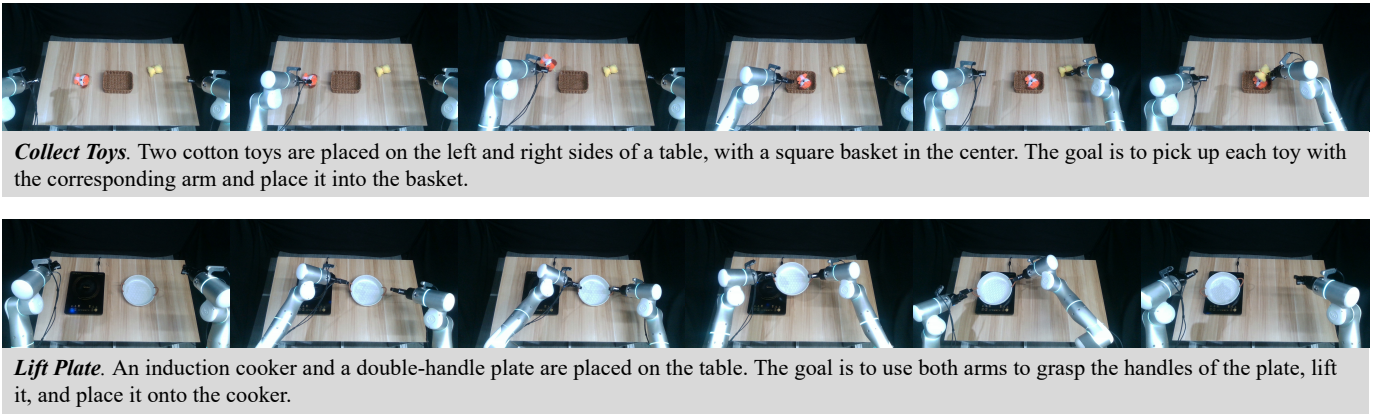


**Fig. 4: Tasks.** We design two tasks to evaluate the in-domain and generalization capabilities of the *RISE-2* policy. Additionally, we assess the ability of the *AirExo-2* system to transform high-quality pseudo-robot demonstrations derived from in-the-wild data. These transformed demonstrations are then used to train downstream policies, allowing us to evaluate their transferability to real robot platforms.

- Q4.** Can generalizable policies like *RISE-2*, trained exclusively on pseudo-robot demonstrations collected and transformed by the *AirExo-2* system, be directly deployed on a real robot?
- Q5.** How important is the demonstration adaptor of the *AirExo-2* system for transferring policies trained solely on in-the-wild demonstrations to a real robot platform?
- Q6.** Can the combination of the *AirExo-2* system and the *RISE-2* policy enable the robot to perform more diverse and complex robotic manipulation tasks?

#### A. Setup

**Platform.** Our dual-arm robot platform uses two Flexiv Rizon 4 robotic arms, each equipped with a Robotiq 2F-85 gripper. An Intel RealSense D415 camera is mounted on top of the robot platform to capture global observations, while two additional Intel RealSense D415 cameras are mounted on the wrists of each robot arm to provide in-hand observations for 2D image-based policies as additional views.

**Tasks.** As shown in Fig. 4, we designed two tasks to evaluate the in-domain and generalization performance of the *RISE-2* policy, as well as to assess the overall effectiveness of the *AirExo-2* system in transferring policies of different tasks trained on in-the-wild demonstrations to a real robot.

**Data Collection.** The teleoperated demonstrations are collected using AirExo [26], while the in-the-wild demonstrations are gathered and transformed through our proposed *AirExo-2* system. For each task, we collect 50 teleoperated demonstrations for policy evaluation and 50 in-the-wild demonstrations to test whether a generalizable policy can be zero-shot deployed to the robot platform using the in-the-wild demonstrations collected and processed by *AirExo-2*.

**Baselines.** We compare *RISE-2* against a range of representative policies based on 2D images and 3D point clouds, including: (1) **ACT** [116], which employs transformers to map image observations and proprioception to robot action chunks; (2) **Diffusion Policy (DP)** [17], which formulates action prediction as a diffusion denoising process [34, 86] conditioned on the image observations; (3) **CAGE** [105], an extension of

DP that incorporates visual foundation models [70], a causal observation perceiver [41], and an attention-based diffusion action head for improved generalization; and (4) **RISE** [96], a 3D imitation policy that leverages a sparse 3D encoder for efficient point cloud perception.

**Evaluation Protocols.** All policies are deployed on a workstation with an NVIDIA RTX 2060 SUPER GPU. Following the procedure outlined in [18, 105], we adopt a consistent evaluation method for each policy to minimize performance variation and ensure reproducibility. Specifically, we generate uniformly distributed test positions randomly before each task evaluation. The workspace is set up identically across different policies and test environments, and success rates are recorded for each test case. Each policy is evaluated over 20 consecutive trials per task, and the success rates are computed accordingly.

#### B. Case Study: Are In-Hand Cameras Sufficient?

We conducted a case study to investigate whether in-hand cameras are sufficient for many manipulation tasks. We select the *Collect Toys* task as an example and utilize CAGE [105] as the policy for this case study.

Method	# Cameras	Success Rate
CAGE (global only)	1	45.0%
CAGE (in-hand only)	2	60.0%
CAGE (global + in-hand)	3	72.5%

**TABLE I: Case Study Results.** In this case study, we employ CAGE with relative action representations following its original implementation [105]. The in-domain and generalization experiments afterward will use CAGE with absolute action representations. For details about action representations, please refer to Appendix F.

**In-hand cameras alone are often insufficient for manipulation tasks and may pose additional obstacles on policy learning (Q1).** As shown in Tab. I, neither global nor in-hand cameras alone provide adequate observations for 2D image-based policies to achieve strong performance. Recent work [96] has demonstrated that using only a global camera enables a 3D imitation policy to outperform 2D multi-view image-based policies, highlighting the importance of 3D

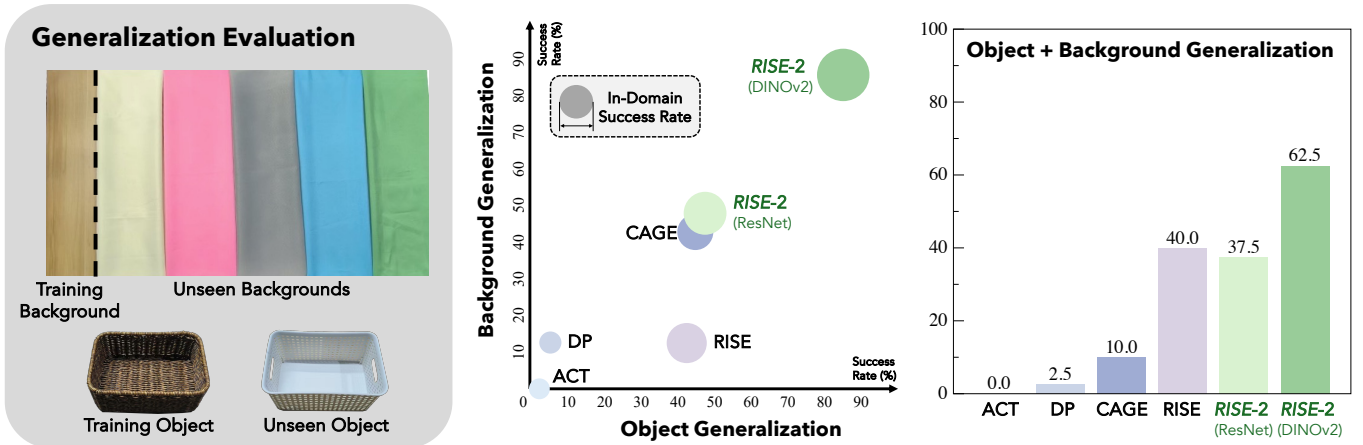


**Fig. 5: Generalization Evaluation Setup and Results.** (Left) We use five unseen backgrounds and one unseen target object to evaluate the generalization ability of the imitation policies. The policies are trained on demonstrations in a narrow domain, which consists of a single training background and target object. (Middle) When only the object or background is replaced, *RISE-2* maintains strong performance with a minimal drop of 10%. (Right) In more challenging scenarios, where both the object and background are replaced with unseen ones, *RISE-2* still demonstrates notable generalization capabilities.

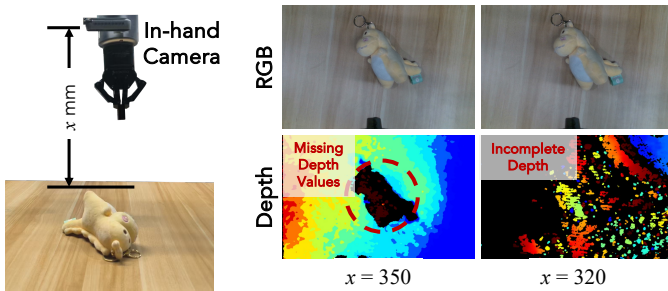


**Fig. 6: Visualization of In-hand Camera Observation.** In-hand cameras often produce low-quality depth observations during interactions with objects, limiting their usages for most 3D point cloud-based policies.

information for scene understanding. However, as illustrated in Fig. 6, in-hand cameras may produce incomplete depth information when the robotic arm approaches an object, making them unsuitable for 3D point-cloud-based policies. Consequently, relying solely on in-hand cameras can degrade the performance of the policies, particularly for 3D policies that rely on complete and accurate depth information to achieve superior performance.

### C. Policy In-Domain Evaluation: *RISE-2*

Method	<i>Collect Toys</i>			<i>Lift Plate</i>	
	Overall	Left	Right	Grasp	Place
ACT [116]	32.5%	50%	15%	45%	20%
DP [17]	40.0%	25%	55%	30%	30%
CAGE [105]	65.0%	70%	60%	55%	55%
RISE [96]	72.5%	60%	85%	75%	75%
<b><i>RISE-2 (ours)</i></b>	<b>95.0%</b>	<b>90%</b>	<b>100%</b>	<b>85%</b>	<b>85%</b>

**TABLE II: In-Domain Evaluation Results of Different Policies on the *Collect Toys* and the *Lift Plate* Task.** Our *RISE-2* policy outperforms baselines during in-domain evaluations.

*RISE-2* achieves significantly better performance than previous policies during in-domain evaluations (Q2). Tab. II reports the success rates for both tasks, highlighting the effectiveness of *RISE-2* in handling diverse manipulation challenges. In the *Collect Toys* task, *RISE-2* consistently outperforms all baselines across both arms, leading to a substantially higher overall success rate. This shows the capability of *RISE* in achieving Similarly, in the *Lift Plate* task, which requires precise motion execution, *RISE-2* demonstrates superior accuracy in predicting fine-grained robotic actions, surpassing all baselines. These results show that *RISE-2* not only improves overall task success but also enhances control precision, making it suitable for complex manipulation scenarios.

The improvement of *RISE-2* over *RISE* also showcases the significance of using separate 2D and 3D encoders along with spatial feature alignment. This design effectively decouples geometric and semantic feature extraction, allowing them to be seamlessly integrated through coordinate-based fusion via spatial aligner, leading to more accurate and robust representations for manipulation tasks.

### D. Policy Generalization Evaluation: *RISE-2*

We select the *Collect Toys* task to conduct a generalization experiment to evaluate the robustness of different policies under varying levels of environmental disturbances. As illustrated in Fig. 5 (left), we introduce two types of disturbances: background variations and object differences. To further investigate the role of disentangling geometric and semantic features in generalization and assess the impact of different visual backbones for semantic feature extraction, we include a variant of *RISE-2* that replaces the DINOv2 encoder with a ResNet-18 encoder [30]. We then follow the same evaluation protocol to compute success rates, enabling a comprehensive comparison of each policy’s generalization capability.

*RISE-2* exhibits strong generalization performance to different environmental disturbances (Q3). As shown in

Fig. 5 (middle), under single disturbances such as background or object replacement, *RISE-2* maintains high performance, experiencing only a 10% success rate drop while still significantly outperforming previous methods. Notably, even when the DINOv2 encoder is replaced with a vanilla ResNet-18 encoder, although the performance is lower than the original *RISE-2*, it still demonstrates a reasonable level of generalization ability and surpasses baseline policies. This result further validates our design choice of employing separate encoders for 3D geometric and 2D semantic feature extraction, effectively enhancing policy robustness. To achieve even better generalization performance under disturbances, using visual foundation models like DINOv2 [70] as 2D dense encoders is essential, as they can leverage the extensive semantic knowledge acquired through large-scale pre-training. This allows for the extraction of more generalizable features from the manipulation scene, ultimately elevating the generalization ability of *RISE-2*.

*RISE-2* even shows decent generalization performance when facing a combination of disturbances (Q3). The results in Fig. 5 (right) show that *RISE-2* retains its generalization performance to a large extent even under combined disturbances. RISE [96] performs unexpectedly well under the combined disturbances, even surpassing its performance when only object replacement is applied. By observing the experimental process, we hypothesize that different disturbances may introduce different offsets in the predicted action of RISE, and sometimes, combining these disturbances may cause the offsets to cancel each other out, leading to unexpectedly good performance. Instead, *RISE-2* does not exhibit this phenomenon, as it consistently demonstrates strong performance across all types of generalization experiments, regardless of the disturbance combination.

#### E. System Evaluation: *AirExo-2*

Our previous experiments have shown that *RISE-2* is a generalizable policy, making it ideal for learning from in-the-wild demonstrations collected and transformed by *AirExo-2*. Accordingly, we train the policy using the pseudo-robot demonstrations processed by *AirExo-2*, and then zero-shot deploy the trained policy on the dual-arm robot platform, without using any additional robot demonstrations. For comparison, we also include RISE [96] in this experiment.

The *AirExo-2* system provides high-quality pseudo-robot demonstrations that can be directly used to train generalizable policies like *RISE-2*, enabling successful zero-shot deployment of the trained policies to the real robot platform with reasonable performance (Q4). As shown in Fig. 7, *RISE-2* performs well when trained solely on pseudo-robot demonstrations collected and transformed by the *AirExo-2* system. The policy achieves satisfactory success rates for both tasks, with only a slight performance drop compared to learning from teleoperated demonstrations. Another policy, RISE, also shows good performance when deployed zero-shot, though with a slightly larger performance drop than *RISE-2*. These results underscore the importance

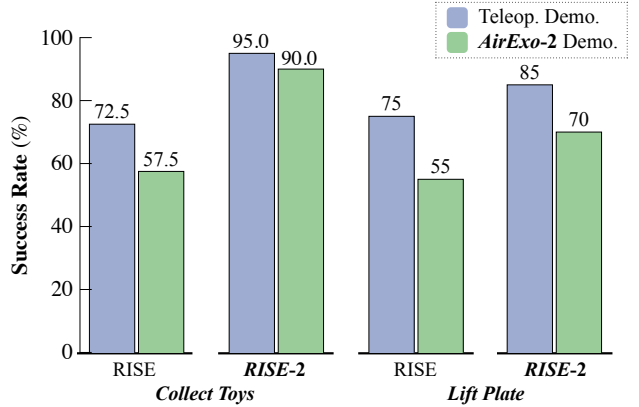


**Fig. 7: System Evaluation Results.** Trained using demonstrations collected and adapted by the *AirExo-2* system, without any access to robot data, the policies maintain reasonable performance, highlighting the overall effectiveness of the *AirExo-2* system.

Method	Success Rate (%)	
	w.o. adaptor	w. adaptor
RISE [96]	30.0%	57.5%
<i>RISE-2</i> (ours)	52.5%	90.0%

**TABLE III: Ablation Results of Demonstration Adaptors.** While generalizable policies trained with raw in-the-wild demonstrations can occasionally transfer to real robot platforms, the inherent embodiment gap hinders their performance. Our proposed demonstration adaptor, especially visual adaptors, effectively bridges this domain gap and enhances the performance of policies during direct transfer, demonstrating its importance in this process.

of having a generalizable policy for transferring manipulation skills learned from in-the-wild demonstrations to real robot environments, in the absence of teleoperation data.

The demonstration adaptor of *AirExo-2* are necessary for achieving satisfactory policy transfer (Q5). We use the *Collect Toys* task to illustrate the importance of the demonstration adaptor in learning from in-the-wild demonstrations. Operation space adaptors are necessary for policy transfer, so we include them in each variant and ablate whether to use visual adaptors (image adaptor and depth adaptor) to transform visual observations into the robot domain. As shown in Tab. III, performance drops significantly when learning directly from raw in-the-wild demonstrations without visual adaptors, indicating that the visual gap between in-the-wild and robot demonstrations is substantial and cannot be ignored. Despite this gap, our *RISE-2* policy still achieves performance comparable to RISE even without demonstration adaptors (52.5% v.s. 57.5%), showcasing its strong generalization ability in learning from cross-embodiment data. These results also validate the authenticity and reliability of the pseudo-robot demonstrations transformed by *AirExo-2*, confirming that they accurately capture real-world interactions and are effective for training generalizable policies. This highlights the potential of combining *RISE-2* and *AirExo-2* as a scalable framework for imitation learning using in-the-wild demonstrations.

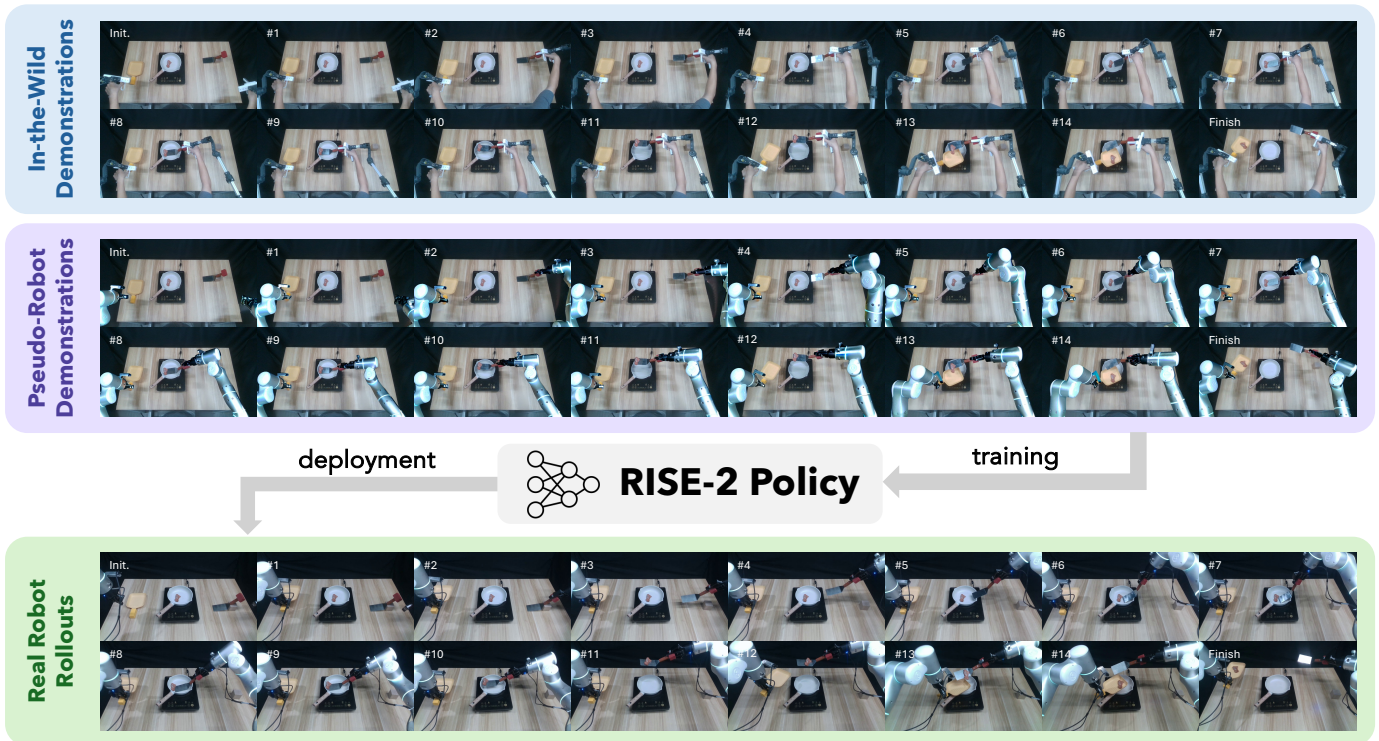


**Fig. 8: Qualitative Results of the *Serve Steak* Task.** The system is evaluated on a challenging, long-horizon, and contact-rich task, *Serve Steak*, in which the robot needs to scoop a steak from a pan using a spatula and slide it onto a plate. This task requires precise control across multiple complex steps. We first collect in-the-wild human demonstrations (top) and convert them into pseudo-robot demonstrations (middle) using *AirExo-2*. These demonstrations are then used to train the *RISE-2* policy, which is successfully deployed on a real robot to complete the task autonomously (bottom).

#### F. Qualitative Results on Challenging Tasks

We additionally evaluate the whole system on a challenging long-horizon and contact-rich task *Serve Steak*, as shown in Fig. 8. This task involves multiple challenging steps that require intricate robot actions: (1) grasp the plate using the left arm; (2) grasp the spatula using the right arm; (3) scoop up the steak in a pan with the grasped spatula; (4) lift the steak with the spatula and slide it onto the plate.

**The integration of the *AirExo-2* system with the *RISE-2* policy enables the robot to tackle the challenging, long-horizon, and contact-rich task without requiring robot demonstrations, highlighting its potential for a wide range of manipulation tasks (Q6).** After training *RISE-2* with only 50 in-the-wild demonstrations collected and processed by *AirExo-2*, we successfully deployed the policy on a real-world robot platform, where it can complete the entire task automatically with no robot data, as illustrated in Fig. 8. This result underscores the effectiveness of the proposed system in learning from a limited number of human demonstrations while generalizing to real-world scenarios, demonstrating its applicability to various complex manipulation tasks.

Notably, we expect the system’s performance to further improve as we scale up in-the-wild demonstrations. The synergy between scalable data collection (*AirExo-2*) and generalizable policy learning (*RISE-2*) suggests a promising trajectory toward more efficient and generalizable robotic manipulation.

Expanding this approach could enable autonomous robots to acquire increasingly complex skills with minimal human supervision, unlocking new possibilities for deployment in real-world environments with high variability and task diversity.

## VI. SYSTEM ANALYSIS

In this section, we conduct thorough analyses of our proposed *AirExo-2* system, including:

- A1.** Is *AirExo-2* easy to use for in-the-wild data collection?
- A2.** How does the data collection speed of *AirExo-2* compare to the data collection speed of teleoperation?
- A3.** How accurate is the *AirExo-2* system in recording actions compared to previous handheld devices used for in-the-wild demonstrations?

### A. User Study

We conduct a user study to comprehensively evaluate the intuitiveness and data throughput of several demonstration collection methods, including end-effector pose teleoperation with haptic device [25], joint-space teleoperation with *AirExo* [26], and *AirExo-2* in-the-wild data collection. The study involves 20 participants with varying levels of experience in robot demonstration collection, including 14 men and 6 women, aged between 21 and 35 years old. The participants are asked to collect one demonstration for the *Collect Toys* task using all three data collection platforms

mentioned above. Before collection, participants are given 3 minutes to familiarize themselves with each data collection platform. We then record the time each participant spends collecting one demonstration. After completing the collection, we designed a questionnaire to gather their feedback on the three data collection methods.

Method	Completion Time (s) ↓	Average Rank ↓		Preference Score ↑
		Intuitiveness	Learnability	
EE pose teleop	46.06 $\pm$ 27.21	3.00 / 3	2.95 / 3	29.75
joint-space teleop	17.31 $\pm$ 5.055	1.80 / 3	2.00 / 3	49.58
<b>AirExo-2 (ours)</b>	<b>5.66<math>\pm</math>1.978</b>	<b>1.20 / 3</b>	<b>1.05 / 3</b>	<b>83.00</b>

TABLE IV: User Study Results. Collecting in-the-wild demonstrations with *AirExo-2* enhances intuitiveness and enables higher data throughput. Users assign higher preference scores to *AirExo-2* compared to other teleoperation data collection methods.

The *AirExo-2* system is intuitive and user-friendly, making it a good choice for large-scale demonstration collection (A1). From Tab. IV we can observe that both experienced participants and novices in demonstration collection find *AirExo-2* more intuitive and easier to learn than teleoperation. Participants significantly prefer *AirExo-2* for in-the-wild collection over both joint-space and end-effector pose teleoperation. This ease of use translates to faster onboarding and smoother operation, making it an excellent tool for diverse users and ensuring more efficient data collection in real-world environments. We believe that the accessibility of *AirExo-2* contributes to more consistent and high-quality demonstrations, reinforcing its value for large-scale, real-world tasks.

Collecting demonstrations with *AirExo-2* is more efficient compared to teleoperation (A2). We assume that the task completion times for different data collection methods follow Gaussian distributions, which is supported by the Shapiro-Wilk test results. To compare the efficiency of in-the-wild demonstration collection with *AirExo-2* versus teleoperated demonstration collection with AirExo, we conduct Welch’s  $t$ -test. Based on the results presented in Tab. IV, we find that *AirExo-2* significantly outperforms AirExo joint-space teleoperation in terms of time efficiency, with a  $p$ -value of  $8.32 \times 10^{-10} < 0.001$ . Additionally, end-effector pose teleoperation is found to be the least efficient for collecting demonstrations. This highlights the advantage of *AirExo-2* in streamlining the data collection process and improving the overall efficiency of task demonstrations.

### B. Accuracy Analysis

Action accuracy is crucial for directly learning from in-the-wild demonstrations, ensuring that the policy can learn precise actions necessary for successful task execution. Handheld devices [18, 22, 82, 83, 109] typically rely on visual SLAM for camera pose trajectory estimation, whereas our *AirExo-2* system leverages its mechanical design and forward kinematics to calculate the robot end-effector trajectory. In this analysis, we select UMI [18] as a representative handheld data collection device and compare its action accuracy with

that of our *AirExo-2* system. We have designed 3 tracks to evaluate the translation accuracies of both systems. Please refer to Appendix G for more details.

Device	Average Error (mm) ↓			Max Error (mm) ↓
	Track 1	Track 2	Track 3	
UMI [18]	7.476 $\pm$ 1.840	10.665 $\pm$ 4.543	8.360 $\pm$ 2.381	20.002
<b>AirExo-2 (ours)</b>	<b>1.213<math>\pm</math>1.332</b>	<b>1.952<math>\pm</math>0.744</b>	<b>1.903<math>\pm</math>1.736</b>	<b>6.134</b>

TABLE V: Action Accuracies of Different In-the-Wild Demonstration Collection Systems. *AirExo-2* exhibits superior action accuracies compared to handheld devices like UMI.

The *AirExo-2* system demonstrates superior accuracy in recording actions compared to handheld devices, making it well-suited for in-the-wild demonstration collection across a wide range of manipulation tasks (A4). The error results in Tab. V show that *AirExo-2* achieves significantly lower action errors (approximately 2mm on average) compared to UMI [18], which relies on visual SLAM and IMU sensors for camera pose estimation. This highlights the advantage of *AirExo-2*, as its mechanical design and forward kinematics provide higher precision than vision-based SLAM methods. These findings confirm that *AirExo-2* is a reliable and accurate tool for capturing high-fidelity motion data, making it an effective solution for large-scale in-the-wild demonstration collection, particularly for fine-grained manipulation tasks that require high precision.

## VII. LIMITATIONS AND FUTURE WORKS

While we utilize the proposed demonstration adaptor to visually transform in-the-wild demonstrations collected by *AirExo-2* into pseudo-robot demonstrations, these transformed demonstrations are primarily useful for generalizable policies. To enhance the applicability of the pseudo-robot demonstrations to a broader range of policies, future work could explore the integration of demonstration augmentation methods, such as novel view synthesis [12, 80, 88, 89], into the demonstration adaptor to improve the diversity of the demonstrations, making them more versatile for various policy learning.

As demonstrated by several works [18, 38, 51, 109], the in-hand image is a semi-unified observation modality across different embodiments. Our case study also reveals that combining in-hand observations can strengthen the performance of various 2D policies. However, the current *AirExo-2* system does not include in-hand cameras. Although we have designed connectors to integrate them with the exoskeleton, calibrating the in-hand cameras with the exoskeleton remains challenging, making it difficult to adapt the in-hand images into the robot domain. Future work could explore effective methods for adapting in-hand images collected by *AirExo-2* to the robot domain, or investigate strategies for leveraging the semi-unified in-hand observations in policy design.

Another limitation lies in the end-effector. The current *AirExo-2* system only supports parallel grippers as end-effectors, limiting its applicability in more dexterous tasks. Future work could integrate the *AirExo-2* system with dexterous

hands and their corresponding exoskeletons, enabling more complex manipulation capabilities and expanding the range of tasks the system can effectively perform.

## VIII. CONCLUSION

This paper introduces *AirExo-2*, a novel system designed for large-scale in-the-wild demonstration collection and adaptation using low-cost exoskeletons. By incorporating a demonstration adaptor, *AirExo-2* enables the visual and kinematic transformation of in-the-wild demonstrations into pseudo-robot demonstrations, which can then be directly applied to downstream imitation learning tasks. We also propose a generalizable policy, *RISE-2*, which effectively integrates both 2D and 3D perception, demonstrating exceptional performance in both in-domain and out-of-domain scenarios.

Further experiments demonstrate that when trained exclusively on pseudo-robot demonstrations generated by the *AirExo-2* system — without using any robot demonstrations — the policy achieves satisfactory performance during zero-shot deployment on a real-world robot platform. This highlights the potential of combining *AirExo-2* and *RISE-2* as a scalable and promising alternative to traditional teleoperation-imitation pipelines, providing a more efficient, cost-effective solution for large-scale, generalizable robotic imitation learning. Together, these results open new possibilities for transferring manipulation skills from in-the-wild environments to real robots, without the need for extensive robot-centric data collection.

## ACKNOWLEDGMENTS

We would like to thank Peishen Yan and Chunyu Xue at Shanghai Jiao Tong University for their helpful suggestions.

## REFERENCES

- [1] Ezra Ameperosa et al. “RoCoDA: Counterfactual Data Augmentation for Data-Efficient Robot Learning from Demonstrations”. In: *arXiv preprint arXiv:2411.16959* (2024).
- [2] Shikhar Bahl et al. “Affordances from human videos as a versatile representation for robotics”. In: *IEEE/CVF Conference on Computer Vision and Pattern Recognition*. 2023.
- [3] Homanga Bharadhwaj. “Position: scaling simulation is neither necessary nor sufficient for in-the-wild robot manipulation”. In: *Forty-first International Conference on Machine Learning*. 2024.
- [4] Homanga Bharadhwaj et al. “Gen2Act: Human Video Generation in Novel Scenarios enables Generalizable Robot Manipulation”. In: *arXiv preprint arXiv:2409.16283* (2024).
- [5] Homanga Bharadhwaj et al. “RoboAgent: Generalization and Efficiency in Robot Manipulation via Semantic Augmentations and Action Chunking”. In: *IEEE International Conference on Robotics and Automation, ICRA 2024, Yokohama, Japan, May 13-17, 2024*. IEEE, 2024, pp. 4788–4795.
- [6] Kevin Black et al. “ $\pi_0$ : A Vision-Language-Action Flow Model for General Robot Control”. In: *arXiv preprint arXiv:2410.24164* (2024).
- [7] Gary Bradski. “The openCV library.” In: *Dr. Dobb’s Journal: Software Tools for the Professional Programmer* 25.11 (2000), pp. 120–123.
- [8] Anthony Brohan et al. “RT-1: Robotics Transformer for Real-World Control at Scale”. In: *Robotics: Science and Systems*. 2023.

- [9] Kaylee Burns et al. “What Makes Pre-Trained Visual Representations Successful for Robust Manipulation?” In: *arXiv preprint arXiv:2312.12444* (2023).
- [10] Chi-Lam Cheang et al. “Gr-2: A generative video-language-action model with web-scale knowledge for robot manipulation”. In: *arXiv preprint arXiv:2410.06158* (2024).
- [11] Jingjing Chen et al. “Towards Effective Utilization of Mixed-Quality Demonstrations in Robotic Manipulation via Segment-Level Selection and Optimization”. In: *arXiv preprint arXiv:2409.19917* (2024).
- [12] Lawrence Yunliang Chen et al. “RoVi-Aug: Robot and Viewpoint Augmentation for Cross-Embodiment Robot Learning”. In: *Conference on Robot Learning (CoRL)*. 2024.
- [13] Linghao Chen et al. “Easyhec: Accurate and automatic hand-eye calibration via differentiable rendering and space exploration”. In: *IEEE Robotics and Automation Letters* (2023).
- [14] Shizhe Chen et al. “PolarNet: 3D Point Clouds for Language-Guided Robotic Manipulation”. In: *Conference on Robot Learning*. PMLR. 2023, pp. 1761–1781.
- [15] Sirui Chen et al. “Arcap: Collecting high-quality human demonstrations for robot learning with augmented reality feedback”. In: *arXiv preprint arXiv:2410.08464* (2024).
- [16] Xinlei Chen, Saining Xie, and Kaiming He. “An Empirical Study of Training Self-Supervised Vision Transformers”. In: *2021 IEEE/CVF International Conference on Computer Vision, ICCV 2021, Montreal, QC, Canada, October 10-17, 2021*. IEEE, 2021, pp. 9620–9629.
- [17] Cheng Chi et al. “Diffusion Policy: Visuomotor Policy Learning via Action Diffusion”. In: *Robotics: Science and Systems*. 2023.
- [18] Cheng Chi et al. “Universal Manipulation Interface: In-The-Wild Robot Teaching Without In-The-Wild Robots”. In: *Proceedings of Robotics: Science and Systems (RSS)*. 2024.
- [19] Christopher Choy, JunYoung Gwak, and Silvio Savarese. “4D Spatio-Temporal ConvNets: Minkowski Convolutional Neural Networks”. In: *Proceedings of the IEEE/CVF Conference on Computer Vision and Pattern Recognition*. 2019, pp. 3075–3084.
- [20] Open X-Embodiment Collaboration et al. “Open X-Embodiment: Robotic Learning Datasets and RT-X Models”. In: *IEEE International Conference on Robotics and Automation*. 2024, pp. 6892–6903.
- [21] Jiafei Duan et al. “AR2-D2: Training a Robot Without a Robot”. In: *Conference on Robot Learning*. Vol. 229. Proceedings of Machine Learning Research. PMLR, 2023, pp. 2838–2848.
- [22] Haritheja Etukuru et al. “Robot Utility Models: General Policies for Zero-Shot Deployment in New Environments”. In: *arXiv preprint arXiv:2409.05865* (2024).
- [23] Hao-Shu Fang et al. “AnyGrasp: Robust and Efficient Grasp Perception in Spatial and Temporal Domains”. In: *IEEE Transactions on Robotics* (2023).
- [24] Hao-Shu Fang et al. “Graspnet-1billion: A large-scale benchmark for general object grasping”. In: *Proceedings of the IEEE/CVF conference on computer vision and pattern recognition*. 2020, pp. 11444–11453.
- [25] Hao-Shu Fang et al. “RH20T: A Comprehensive Robotic Dataset for Learning Diverse Skills in One-Shot”. In: *IEEE International Conference on Robotics and Automation, ICRA 2024, Yokohama, Japan, May 13-17, 2024*. IEEE, 2024, pp. 653–660.
- [26] Hongjie Fang et al. “AirExo: Low-Cost Exoskeletons for Learning Whole-Arm Manipulation in the Wild”. In: *IEEE International Conference on Robotics and Automation (ICRA)*. IEEE. 2024, pp. 15031–15038.
- [27] Théophile Gervet et al. “Act3D: 3D Feature Field Transformers for Multi-Task Robotic Manipulation”. In: *Confer-*

- ence on Robot Learning, CoRL 2023, 6-9 November 2023, Atlanta, GA, USA. Ed. by Jie Tan, Marc Toussaint, and Kourosh Darvish. Vol. 229. Proceedings of Machine Learning Research. PMLR, 2023, pp. 3949–3965.
- [28] Ankit Goyal et al. “RVT: Robotic View Transformer for 3D Object Manipulation”. In: *Conference on Robot Learning*. PMLR, 2023, pp. 694–710.
- [29] Haoran He et al. “Large-scale actionless video pre-training via discrete diffusion for efficient policy learning”. In: *arXiv preprint arXiv:2402.14407* (2024).
- [30] Kaiming He et al. “Deep Residual Learning for Image Recognition”. In: *Proceedings of the IEEE Conference on Computer Vision and Pattern Recognition*. 2016, pp. 770–778.
- [31] Tom Henighan et al. “Scaling laws for autoregressive generative modeling”. In: *arXiv preprint arXiv:2010.14701* (2020).
- [32] Nick Heppert et al. “DITTO: Demonstration Imitation by Trajectory Transformation”. In: *arXiv preprint arXiv:2403.15203* (2024).
- [33] Jonathan Ho, Ajay Jain, and Pieter Abbeel. “Denosing Diffusion Probabilistic Models”. In: *Advances in Neural Information Processing Systems* 33 (2020), pp. 6840–6851.
- [34] Jonathan Ho, Ajay Jain, and Pieter Abbeel. “Denosing Diffusion Probabilistic Models”. In: *Advances in Neural Information Processing Systems* 33 (2020), pp. 6840–6851.
- [35] Jonathan Ho and Tim Salimans. “Classifier-free diffusion guidance”. In: *arXiv preprint arXiv:2207.12598* (2022).
- [36] Zhengdong Hong, Kangfu Zheng, and Linghao Chen. “Fully Automatic Hand-Eye Calibration with Pretrained Image Models”. In: *International Conference on Intelligent Robots and Systems (IROS)* (2024).
- [37] Ryan Hoque et al. “IntervenGen: Interventional Data Generation for Robust and Data-Efficient Robot Imitation Learning”. In: *arXiv preprint arXiv:2405.01472* (2024).
- [38] Kyle Hsu et al. “Vision-Based Manipulators Need to Also See from Their Hands”. In: *ICLR*. OpenReview.net, 2022.
- [39] Edward J. Hu et al. “LoRA: Low-Rank Adaptation of Large Language Models”. In: *The Tenth International Conference on Learning Representations, ICLR 2022, Virtual Event, April 25-29, 2022*. OpenReview.net, 2022.
- [40] Pu Hua et al. “Gensim2: Scaling robot data generation with multi-modal and reasoning llms”. In: *arXiv preprint arXiv:2410.03645* (2024).
- [41] Andrew Jaegle et al. “Perceiver IO: A General Architecture for Structured Inputs & Outputs”. In: *International Conference on Learning Representations*. 2022.
- [42] Eric Jang et al. “BC-Z: Zero-Shot Task Generalization with Robotic Imitation Learning”. In: *Conference on Robot Learning*. PMLR, 2021, pp. 991–1002.
- [43] Michael Janner et al. “Planning with Diffusion for Flexible Behavior Synthesis”. In: *International Conference on Machine Learning*. PMLR, 2022, pp. 9902–9915.
- [44] Yueru Jia et al. “Lift3D Foundation Policy: Lifting 2D Large-Scale Pretrained Models for Robust 3D Robotic Manipulation”. In: *arXiv preprint arXiv:2411.18623* (2024).
- [45] Zhenyu Jiang et al. “DexMimicGen: Automated Data Generation for Bimanual Dexterous Manipulation via Imitation Learning”. In: *arXiv preprint arXiv:2410.24185* (2024).
- [46] Jared Kaplan et al. “Scaling laws for neural language models”. In: *arXiv preprint arXiv:2001.08361* (2020).
- [47] Simar Kaeer et al. “Egomimic: Scaling imitation learning via egocentric video”. In: *arXiv preprint arXiv:2410.24221* (2024).
- [48] Hiroharu Kato et al. “Differentiable rendering: A survey”. In: *arXiv preprint arXiv:2006.12057* (2020).
- [49] Alexander Khazatsky et al. “DROID: A large-scale in-the-wild robot manipulation dataset”. In: *Robotics: Science and Systems*. 2024.
- [50] Heecheol Kim et al. “Training robots without robots: deep imitation learning for master-to-robot policy transfer”. In: *IEEE Robotics and Automation Letters* 8.5 (2023), pp. 2906–2913.
- [51] Moo Jin Kim, Jiajun Wu, and Chelsea Finn. “Giving robots a hand: Learning generalizable manipulation with eye-in-hand human video demonstrations”. In: *arXiv preprint arXiv:2307.05959* (2023).
- [52] Moo Jin Kim et al. “OpenVLA: An Open-Source Vision-Language-Action Model”. In: *arXiv preprint arXiv:2406.09246* (2024).
- [53] Diederik P Kingma. “Adam: A method for stochastic optimization”. In: *arXiv preprint arXiv:1412.6980* (2014).
- [54] Alexander Kirillov et al. “Segment anything”. In: *Proceedings of the IEEE/CVF International Conference on Computer Vision*. 2023, pp. 4015–4026.
- [55] Tzu-Mao Li et al. “Differentiable Monte Carlo Ray Tracing through Edge Sampling”. In: *ACM Trans. Graph. (Proc. SIGGRAPH Asia)* 37.6 (2018), 222:1–222:11.
- [56] Fanqi Lin et al. “Data scaling laws in imitation learning for robotic manipulation”. In: *arXiv preprint arXiv:2410.18647* (2024).
- [57] Xingyu Lin et al. “SpawnNet: Learning Generalizable Visuomotor Skills from Pre-trained Network”. In: *IEEE International Conference on Robotics and Automation, ICRA 2024, Yokohama, Japan, May 13-17, 2024*. IEEE, 2024, pp. 4781–4787.
- [58] Songming Liu et al. “Rdt-1b: a diffusion foundation model for bimanual manipulation”. In: *arXiv preprint arXiv:2410.07864* (2024).
- [59] Wenhai Liu et al. “ForceMimic: Force-Centric Imitation Learning with Force-Motion Capture System for Contact-Rich Manipulation”. In: *arXiv preprint arXiv:2410.07554* (2024).
- [60] Shengcheng Luo et al. “Human-agent joint learning for efficient robot manipulation skill acquisition”. In: *arXiv preprint arXiv:2407.00299* (2024).
- [61] Jun Lv et al. “SAM-RL: Sensing-Aware Model-Based Reinforcement Learning via Differentiable Physics-Based Simulation and Rendering”. In: *Robotics: Science and Systems*. 2023.
- [62] Yecheng Jason Ma et al. “LIV: Language-Image Representations and Rewards for Robotic Control”. In: *International Conference on Machine Learning*. PMLR, 2023, pp. 23301–23320.
- [63] Yecheng Jason Ma et al. “VIP: Towards Universal Visual Reward and Representation via Value-Implicit Pre-Training”. In: *International Conference on Learning Representations*. 2023.
- [64] Arjun Majumdar et al. “Where are We in the Search for an Artificial Visual Cortex for Embodied Intelligence?” In: *ICRA 2023 Workshop on Pretraining for Robotics*. 2023.
- [65] Ajay Mandlekar et al. “MimicGen: A Data Generation System for Scalable Robot Learning using Human Demonstrations”. In: *Conference on Robot Learning*. Vol. 229. Proceedings of Machine Learning Research. PMLR, 2023, pp. 1820–1864.
- [66] Robert McCarthy et al. “Towards Generalist Robot Learning from Internet Video: A Survey”. In: *arXiv preprint arXiv:2404.19664* (2024).
- [67] Yao Mu et al. “Robotwin: Dual-arm robot benchmark with generative digital twins”. In: *arXiv preprint arXiv:2409.02920* (2024).
- [68] Suraj Nair et al. “R3M: A Universal Visual Representation for Robot Manipulation”. In: *Conference on Robot Learning*. PMLR, 2022, pp. 892–909.

- [69] Octo Model Team et al. “Octo: An Open-Source Generalist Robot Policy”. In: *Proceedings of Robotics: Science and Systems (RSS)*. 2024.
- [70] Maxime Oquab et al. “DINOv2: Learning Robust Visual Features without Supervision”. In: *Trans. Mach. Learn. Res.* 2024 (2024).
- [71] Georgios Papagiannis et al. “R+ x: Retrieval and execution from everyday human videos”. In: *arXiv preprint arXiv:2407.12957* (2024).
- [72] William Peebles and Saining Xie. “Scalable diffusion models with transformers”. In: *Proceedings of the IEEE/CVF International Conference on Computer Vision*. 2023, pp. 4195–4205.
- [73] Dean Pomerleau. “ALVINN: An Autonomous Land Vehicle in a Neural Network”. In: *Advances in Neural Information Processing Systems 1, [NIPS Conference, Denver, Colorado, USA, 1988]*. Ed. by David S. Touretzky. Morgan Kaufmann, 1988, pp. 305–313.
- [74] Jianing Qian, Anastasios Panagopoulos, and Dinesh Jayaraman. “Recasting Generic Pretrained Vision Transformers As Object-Centric Scene Encoders For Manipulation Policies”. In: *IEEE International Conference on Robotics and Automation, ICRA 2024, Yokohama, Japan, May 13-17, 2024*. IEEE, 2024, pp. 17544–17552.
- [75] Yuzhe Qin et al. “Dexmv: Imitation learning for dexterous manipulation from human videos”. In: *European Conference on Computer Vision*. Springer, 2022, pp. 570–587.
- [76] Alec Radford et al. “Learning Transferable Visual Models From Natural Language Supervision”. In: *Proceedings of the 38th International Conference on Machine Learning, ICML 2021, 18-24 July 2021, Virtual Event*. Ed. by Marina Meila and Tong Zhang. Vol. 139. Proceedings of Machine Learning Research. PMLR, 2021, pp. 8748–8763.
- [77] Ilija Radosavovic et al. “Real-World Robot Learning with Masked Visual Pre-Training”. In: *Conference on Robot Learning*. PMLR, 2022, pp. 416–426.
- [78] Nikhila Ravi et al. “Sam 2: Segment anything in images and videos”. In: *arXiv preprint arXiv:2408.00714* (2024).
- [79] Robin Rombach et al. “High-Resolution Image Synthesis With Latent Diffusion Models”. In: *Proceedings of the IEEE/CVF Conference on Computer Vision and Pattern Recognition (CVPR)*. 2022, pp. 10684–10695.
- [80] Kyle Sargent et al. “ZeroNVS: Zero-Shot 360-Degree View Synthesis from a Single Image”. In: *Proceedings of the IEEE/CVF Conference on Computer Vision and Pattern Recognition*. 2024, pp. 9420–9429.
- [81] Johannes L Schonberger and Jan-Michael Frahm. “Structure-from-motion revisited”. In: *Proceedings of the IEEE conference on computer vision and pattern recognition*. 2016, pp. 4104–4113.
- [82] Mingyo Seo et al. “LEGATO: Cross-Embodiment Imitation Using a Grasping Tool”. In: *arXiv preprint arXiv:2411.03682* (2024).
- [83] Nur Muhammad Mahi Shafiullah et al. “On bringing robots home”. In: *arXiv preprint arXiv:2311.16098* (2023).
- [84] Mohit Shridhar, Lucas Manuelli, and Dieter Fox. “Perceiver-Actor: A Multi-Task Transformer for Robotic Manipulation”. In: *Conference on Robot Learning, CoRL 2022, 14-18 December 2022, Auckland, New Zealand*. Ed. by Karen Liu, Dana Kulic, and Jeffrey Ichnowski. Vol. 205. Proceedings of Machine Learning Research. PMLR, 2022, pp. 785–799.
- [85] Laura M. Smith et al. “AVID: Learning Multi-Stage Tasks via Pixel-Level Translation of Human Videos”. In: *Robotics: Science and Systems*. 2020.
- [86] Jiaming Song, Chenlin Meng, and Stefano Ermon. “Denoising Diffusion Implicit Models”. In: *The International Conference on Learning Representations*. 2021.
- [87] Mohan Kumar Srirama et al. “HRP: Human Affordances for Robotic Pre-Training”. In: *Proceedings of Robotics: Science and Systems*. 2024.
- [88] Stephen Tian et al. “View-Invariant Policy Learning via Zero-Shot Novel View Synthesis”. In: *Conference on Robot Learning (CoRL)*. 2024.
- [89] Basile Van Hoorick et al. “Generative camera dolly: Extreme monocular dynamic novel view synthesis”. In: *European Conference on Computer Vision*. Springer, 2025, pp. 313–331.
- [90] Ashish Vaswani et al. “Attention is All You Need”. In: *Advances in Neural Information Processing Systems 30* (2017).
- [91] Vitalis Vosylius and Edward Johns. “Instant Policy: In-Context Imitation Learning via Graph Diffusion”. In: *arXiv preprint arXiv:2411.12633* (2024).
- [92] Homer Rich Walke et al. “BridgeData V2: A Dataset for Robot Learning at Scale”. In: *Conference on Robot Learning*. Vol. 229. Proceedings of Machine Learning Research. PMLR, 2023, pp. 1723–1736.
- [93] Chen Wang et al. “DexCap: Scalable and Portable Mocap Data Collection System for Dexterous Manipulation”. In: *Robotics: Science and Systems*. 2024.
- [94] Chen Wang et al. “MimicPlay: Long-Horizon Imitation Learning by Watching Human Play”. In: *Conference on Robot Learning (CoRL)*. 2023, pp. 201–221.
- [95] Chenxi Wang et al. “Graspness discovery in cluttered for fast and accurate grasp detection”. In: *Proceedings of the IEEE/CVF International Conference on Computer Vision*. 2021, pp. 15964–15973.
- [96] Chenxi Wang et al. “RISE: 3D Perception Makes Real-World Robot Imitation Simple and Effective”. In: *2024 IEEE/RSJ International Conference on Intelligent Robots and Systems (IROS)*. 2024, pp. 2870–2877.
- [97] Jun Wang et al. “CyberDemo: Augmenting Simulated Human Demonstration for Real-World Dexterous Manipulation”. In: *IEEE/CVF Conference on Computer Vision and Pattern Recognition*. IEEE, 2024, pp. 17952–17963.
- [98] Jun Wang et al. “EVE: Enabling Anyone to Train Robots using Augmented Reality”. In: *Proceedings of the 37th Annual ACM Symposium on User Interface Software and Technology*. 2024, pp. 1–13.
- [99] Lirui Wang et al. “GenSim: Generating Robotic Simulation Tasks via Large Language Models”. In: *International Conference on Learning Representations*. 2024.
- [100] Lirui Wang et al. “Scaling proprioceptive-visual learning with heterogeneous pre-trained transformers”. In: *arXiv preprint arXiv:2409.20537* (2024).
- [101] Yufei Wang et al. “RoboGen: Towards Unleashing Infinite Data for Automated Robot Learning via Generative Simulation”. In: *International Conference on Machine Learning*. 2024.
- [102] Chuan Wen et al. “Any-point trajectory modeling for policy learning”. In: *arXiv preprint arXiv:2401.00025* (2023).
- [103] Hongtao Wu et al. “Unleashing Large-Scale Video Generative Pre-training for Visual Robot Manipulation”. In: *International Conference on Learning Representations*. 2024.
- [104] Kun Wu et al. “RoboMIND: Benchmark on Multi-embodiment Intelligence Normative Data for Robot Manipulation”. In: *arXiv preprint arXiv:2412.13877* (2024).
- [105] Shangning Xia et al. “CAGE: Causal Attention Enables Data-Efficient Generalizable Robotic Manipulation”. In: *arXiv preprint arXiv:2410.14974* (2024).
- [106] Haoyu Xiong et al. “Learning by watching: Physical imitation of manipulation skills from human videos”. In: *2021 IEEE/RSJ International Conference on Intelligent Robots and Systems (IROS)*. IEEE, 2021, pp. 7827–7834.

- [107] Mengda Xu et al. “Flow as the cross-domain manipulation interface”. In: *arXiv preprint arXiv:2407.15208* (2024).
- [108] Seonghyeon Ye et al. “Latent action pretraining from videos”. In: *arXiv preprint arXiv:2410.11758* (2024).
- [109] Sarah Young et al. “Visual Imitation Made Easy”. In: *Conference on Robot Learning*. Vol. 155. Proceedings of Machine Learning Research. PMLR, 2020, pp. 1992–2005.
- [110] Yanjie Ze et al. “3D Diffusion Policy: Generalizable Visuomotor Policy Learning via Simple 3D Representations”. In: *Proceedings of Robotics: Science and Systems (RSS)*. 2024.
- [111] Jia Zeng et al. “Learning Manipulation by Predicting Interaction”. In: *Proceedings of Robotics: Science and Systems*. 2024.
- [112] Junjie Zhang et al. “SAM-E: Leveraging Visual Foundation Model with Sequence Imitation for Embodied Manipulation”. In: *Forty-first International Conference on Machine Learning, ICML 2024, Vienna, Austria, July 21-27, 2024*. OpenReview.net, 2024.
- [113] Lvmin Zhang, Anyi Rao, and Maneesh Agrawala. “Adding conditional control to text-to-image diffusion models”. In: *Proceedings of the IEEE/CVF International Conference on Computer Vision*. 2023, pp. 3836–3847.
- [114] Tong Zhang et al. “A Universal Semantic-Geometric Representation for Robotic Manipulation”. In: *CoRL*. Vol. 229. Proceedings of Machine Learning Research. PMLR, 2023, pp. 3342–3363.
- [115] Tong Zhang et al. “Leveraging Locality to Boost Sample Efficiency in Robotic Manipulation”. In: *arXiv preprint arXiv:2406.10615* (2024).
- [116] Tony Z Zhao et al. “Learning Fine-Grained Bimanual Manipulation with Low-Cost Hardware”. In: *Robotics: Science and Systems*. 2023.
- [117] Qian-Yi Zhou, Jaesik Park, and Vladlen Koltun. “Open3D: A modern library for 3D data processing”. In: *arXiv preprint arXiv:1801.09847* (2018).
- [118] Shangchen Zhou et al. “Propainter: Improving propagation and transformer for video inpainting”. In: *Proceedings of the IEEE/CVF International Conference on Computer Vision*. 2023, pp. 10477–10486.
- [119] Yi Zhou et al. “On the Continuity of Rotation Representations in Neural Networks”. In: *Proceedings of the IEEE/CVF Conference on Computer Vision and Pattern Recognition (CVPR)*. 2019, pp. 5745–5753.
- [120] Brianna Zitkovich et al. “RT-2: Vision-Language-Action Models Transfer Web Knowledge to Robotic Control”. In: *Conference on Robot Learning, CoRL 2023, 6-9 November 2023, Atlanta, GA, USA*. Ed. by Jie Tan, Marc Toussaint, and Kourosh Darvish. Vol. 229. Proceedings of Machine Learning Research. PMLR, 2023, pp. 2165–2183.

### A. *AirExo-2* Hardware Design

To collect in-the-wild data that is easy to transform into pseudo robotic data, a highly precise data collection system is essential to ensure demonstration quality for downstream policy learning. From the hardware perspective, *AirExo* [26] has several key limitations:

- H1.** Most of its components are 3D-printed using polylactic acid (PLA), leading to low rigidity and susceptibility to structural deformation.
- H2.** Unlike typical robots with constrained ranges, its joints can rotate beyond  $360^\circ$ , potentially reaching positions the robot cannot achieve.
- H3.** Although portable, inevitable body movements during operations can cause its base to shift, leading to inaccurate action recording.
- H4.** Its gripper lacks smooth control, leading to potential jamming under clamping forces.
- H5.** Its shaft connects directly to the encoder, with wires routed along its side. Joint movement can cause constant friction and stretching, risking wire breakage or short circuits over long-time use.

During demonstration collection using teleoperation, most of the above issues (except **H4**) might not significantly impact data acquisition, as the human operator can adjust their actions based on the movements of the robotic arms. However, during the in-the-wild demonstration collection, these drawbacks can substantially affect motion capture accuracy and may result in invalid or unusable demonstration data.

The hardware design of *AirExo-2* is primarily driven by the limitations mentioned above. To ensure seamless integration with the learning process from in-the-wild demonstrations, we design the exoskeleton to match the dimensions of the robotic arm in a 1:1 ratio. This design choice helps avoid unnecessary obstacles in direct learning from the collected demonstrations. The key hardware designs are outlined as follows.

**Enhanced Overall Structural Rigidity (H1).** In *AirExo*, the links connecting two consecutive joints are the most prone to deformation. In *AirExo-2*, we replace the 3D-printed parts with 20x20 European standard aluminum profiles, providing significantly higher strength at a very low cost. For the joints, the outer shell is 3D-printed using PLA-CF, a carbon fiber-reinforced PLA material with higher hardness. Inside the joint, larger bearings are used to further enhance structural rigidity. Together with the improved links, the hardware upgrade significantly increases the overall structural rigidity of *AirExo-2*, making the exoskeleton more durable, and thereby improving data collection accuracy.

**Hollow Rotating Disc and Side-Mounted Encoder (H5).** As shown in Fig. 9, this design features an encoder mounted on the side of the joint, which uses a gear mechanism to translate the rotational angle of the rotating disc into encoder readings. The hollow disc design allows wires to pass through, preventing them from stretching during rotation and thereby

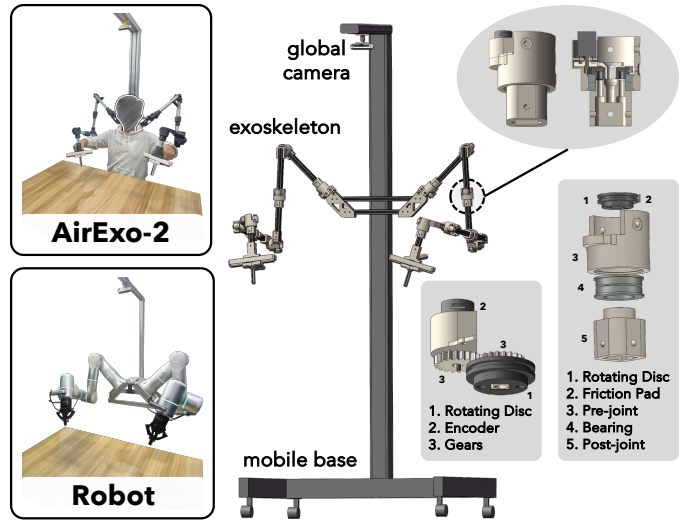


**Fig. 9: Hardware Design of *AirExo-2*.** The *AirExo-2* demonstration collection platform consists of a mobile base and a dual-arm exoskeleton. Global cameras can be mounted on top of the platform to capture visual observations during data collection. The detailed joint structure is shown on the right side, featuring two key designs: hollow rotating disc and side-mounted encoder; joint with angle limit and adjustable friction.

extending their lifespan. Additionally, the side-mounted encoder simplifies maintenance, enabling easy debugging and replacement without the need to disassemble the joint.

**Joint with Angle Limit and Adjustable Friction (H2).** This structure consists of a rotating disc with a grooved track and a friction pad that can be embedded into the track. Together, they allow for adjustment of the limiting angle, ensuring that the motion range of the *AirExo-2* joint exactly aligns with the corresponding joint range of the robot. As illustrated in Fig. 9, the rotating disc, pre-joint, and post-joint are connected through bearings, allowing the rotational motion of the joint to be directly transmitted to the track. For demonstration collection, excessive or insufficient friction in the rotation of the joints is undesirable. Hence, the friction force of the joint in *AirExo-2* can be adjusted by turning the screw on the outer shell, which compresses the friction pad. This design ensures optimal friction for comfortable and accurate data collection.

**Smooth Gripper Control (H4).** Following [18, 59], the gripper of *AirExo-2* incorporates a linear guide, with the fingers mounted on a sliding block. This design allows for smoother opening and closing of the gripper, ensuring it operates seamlessly even under significant clamping forces without any stalling.

**Mobile Data Collection Platform (H3).** Portability is crucial for in-the-wild data collection. However, to address the issue of base movement caused by the body motion of the operator, we mount *AirExo-2* on a mobile aluminum profile stand, as shown in Fig. 9. This setup ensures stability of the base during demonstration collection while maintaining the flexibility needed for mobility, enabling large-scale demonstra-

tion collection in real-world environments. An Intel RealSense D415 camera is set up on the top of the mobile platform to capture global observations. We also designed two optional camera mounts (though not used in this paper) for the future integration of in-hand cameras on the top of both grippers.

### B. AirExo-2 Calibration

The *AirExo-2* system requires two types of calibration simultaneously: (1) aligning the zero positions of each joint with the corresponding robot joint, and (2) determining the transformation between the global camera and the *AirExo-2* base. To address these challenges, we propose a two-stage calibration process.

**Initial Calibration.** For initial calibration, the former calibration can be achieved by manually adjusting the joints to approximate the zero position using specialized 3D-printed tools and reading the encoder values, obtaining  $\{\tilde{q}_{\text{calib}}^{\text{left}}, \tilde{q}_{\text{calib}}^{\text{right}}\}$ . The latter calibration can be done by attaching an ArUco calibration marker board with a known position on the base  $\mathbf{T}_{\text{marker}}^{\text{base}}$  and performing optical calibration using the OpenCV library [7], obtaining  $\mathbf{T}_{\text{marker}}^{\text{camera}}$ . Thus, the transformation can be calculated as

$$\begin{bmatrix} \tilde{\mathbf{r}}_{\text{base}}^{\text{camera}} \\ \tilde{\mathbf{t}}_{\text{base}}^{\text{camera}} \end{bmatrix} \stackrel{\text{def}}{=} \tilde{\mathbf{T}}_{\text{base}}^{\text{camera}} = \mathbf{T}_{\text{marker}}^{\text{camera}} \left( \tilde{\mathbf{T}}_{\text{marker}}^{\text{base}} \right)^{-1} \quad (6)$$

However, this approach introduces errors due to human observation, calibration board misalignment, and optical inaccuracies. In a chained system like *AirExo-2*, these errors may propagate and amplify across joints, leading to significant cumulative inaccuracies in the end-effector pose. Therefore, fine-grained calibration is essential to ensure precise and consistent alignment between *AirExo-2* and the camera frames during demonstration collection.

**Calibration via Differentiable Rendering.** In the second stage, inspired by prior works [13, 36, 61], we use differentiable rendering [48] to refine the initial calibration. Training samples are obtained from a single human *play* trajectory with *AirExo-2*. Using the joint states and calibration parameters, we render the system mask and depth via a differentiable rendering engine [55]. Calibration parameters are optimized by minimizing discrepancies between the rendered and annotated system masks, as well as between the rendered and observed depths. Pseudo-ground-truth masks are manually annotated with SAM-2 [78]. This iterative refinement compensates for errors that accumulate across joints, ultimately improving the overall accuracy.

Specifically, we define  $p$ , the calibration parameters to be optimized through differentiable rendering, as

$$p \stackrel{\text{def}}{=} \{\Delta \mathbf{t}_{\text{base}}^{\text{camera}}, \mathbf{r}_{\text{base}}^{\text{camera}}, \Delta q_{\text{calib}}^{\text{left}}, \Delta q_{\text{calib}}^{\text{right}}\} \quad (7)$$

where parameters, except for the base-to-camera rotation, are represented as deltas relative to the initial calibration results. The base-to-camera rotation is expressed in a 6D format [119]. Thus, the final calibration results can be calculated as

$$\mathbf{T}_{\text{base}}^{\text{camera}} = \begin{bmatrix} \tilde{\mathbf{r}}_{\text{base}}^{\text{camera}} + \Delta \mathbf{t}_{\text{base}}^{\text{camera}} \\ \tilde{\mathbf{t}}_{\text{base}}^{\text{camera}} \end{bmatrix}, \quad (8)$$

$$q_{\text{calib}}^{\text{type}} = \tilde{q}_{\text{calib}}^{\text{type}} + \Delta q_{\text{calib}}^{\text{type}}, \quad \text{type} \in [\text{left}, \text{right}], \quad (9)$$

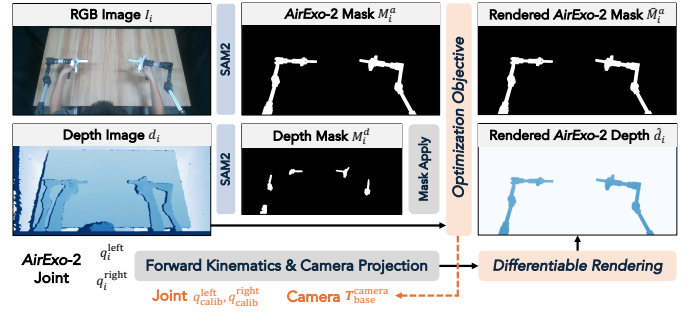


**Fig. 10: Calibration via Differentiable Rendering.** The parameters in orange denote the calibration parameters to be optimized via differentiable rendering.

and the initial parameter values are set as

$$p_0 = \{\mathbf{0}, \tilde{\mathbf{r}}_{\text{base}}^{\text{camera}}, \mathbf{0}, \mathbf{0}\} \quad (10)$$

For the optimization process, we first record a single in-the-wild *play* trajectory, in which the human operator uses the *AirExo-2* to adopt various poses. During trajectory recording, ensure that all parts of the *AirExo-2* remain above the human hands and arms from the camera's perspective. After data collection, we sample approximately 40 image-joint pairs from the trajectory, denoted as  $\{I_i, d_i, q_i^{\text{left}}, q_i^{\text{right}}\}_{i=1}^{N_c}$ , where  $N_c$  represents the total number of training samples for calibration, and  $I_i$  and  $d_i$  are the RGB and depth images of the  $i$ -th sample, respectively. Subsequently, we utilize SAM-2 [78] to annotate the *AirExo-2* mask  $M_i^a$  and the depth mask  $M_i^d \subseteq M_i^a$  for each sample  $i$ , as shown in Fig. 10. The first mask provides supervision for the rendered *AirExo-2* mask, while the second mask is used to select the valid depth information that serves as the supervision signal.

The differentiable rendering engine Redner [55] is employed to render the *AirExo-2* mask  $\hat{M}_i^a$  and *AirExo-2* depth  $\hat{d}_i$  using the calibration results and joint information:

$$\hat{M}_i^a, \hat{d}_i = \mathcal{R}(p; q_i^{\text{left}}, q_i^{\text{right}}, \tilde{\mathbf{T}}_{\text{base}}^{\text{camera}}, \tilde{q}^{\text{left}}, \tilde{q}^{\text{right}}), \quad (11)$$

where the rendering engine  $\mathcal{R}(p; \dots)$  computes the gradients of the calibration parameters  $p$  during the rendering process, and  $\tilde{\mathbf{T}}_{\text{base}}^{\text{camera}}, \tilde{q}^{\text{left}}, \tilde{q}^{\text{right}}$  represent the initial calibration results.

The rendered *AirExo-2* mask  $\hat{M}_i^a$  is supervised by the human-annotated pseudo-*AirExo-2* mask  $M_i^a$ , and the rendered *AirExo-2* depth  $\hat{d}_i$  is supervised by the camera depth  $d_i$  within the region of the human-annotated depth mask  $M_i^d$ . The depth mask ensures that only accurate depth information contributes to the loss. Thus, the objective can be written as:

$$L = \frac{1}{N_c} \sum_{i=1}^{N_c} \left( \beta \cdot \|M_i^a - \hat{M}_i^a\|^2 + \|d_i - \hat{d}_i\|^2 \circ M_i^d \right), \quad (12)$$

where  $\beta$  represents the weighting coefficient, and  $\circ$  denotes the mask-apply operation. In practice, we set  $\beta = 5$ , use  $N_c = 40$  samples for optimization, and employ the Adam optimizer [53] with a learning rate of  $10^{-4}$  for 1000 iterations to fine-tune the calibration results.

### C. Calibration Analysis

Apart from the two-stage calibration process described in Appendix B, we implement several calibration alternatives, including (1) **initial calibration**, which uses the calibration results from the first stage without further fine-tuning; (2) **human annotation**, where a human operator utilizes a real-time GUI program to manually adjust the calibration parameters to align the rendered *AirExo-2* contour with the visually observed contour from camera frames; and (3) **two-stage calibration (mask only)**, which fine-tunes the calibration results by using only mask differences as supervision.

Method	Difference ↓	
	Mask (%)	Depth (mm)
Initial Calibration	1.71±0.37	21.6±5.2
Human Annotation	2.31±0.31	31.2±6.4
Two-Stage Calibration (mask only)	1.10±0.26	17.6±4.1
Two-Stage Calibration (mask + depth)	<b>0.78±0.25</b>	<b>14.0±2.9</b>

**TABLE VI: Calibration Analysis Results.** Using our proposed two-stage calibration, we achieve higher accuracy than both initial calibration and human annotations. Including depth as additional supervision also helps the optimization process convergence.

**Our two-stage calibration process achieves more accurate results compared to other alternatives.** As reported in Tab. VI, our two-stage calibration process achieves the lowest error rates, with a 0.78% mask difference and 14.0 mm depth difference, yielding more precise calibration. It’s worth noticing that the depth difference here does not fully represent action accuracy because commercial depth sensors can produce noisy depth maps. Please refer to §VI-B for more details about action accuracy. Interestingly, human annotation performs even worse than initial calibration, mainly because annotators can only rely on 2D visual information to adjust calibration parameters. This limitation makes it difficult to accurately estimate depth information, leading to larger errors. Conversely, our two-stage calibration process explicitly models 3D information via differentiable rendering, offering a more reliable and precise solution for calibrating the *AirExo-2* system.

### D. Demonstration Adaptor

**Semi-Automatic SAM-2 Annotations.** In the image adaptor, we initially annotate the hand mask (and, if visible, the head mask) manually using SAM-2 [78]. However, after a few annotations, we can fine-tune SAM-2 on the human-annotated samples, enabling automated labeling. This significantly reduces human effort and streamlines the demonstration adaptor process, making it nearly fully automated.

**ControlNet Training.** We train a ControlNet [113] based on the Stable Diffusion 1.5 [79] model to generate photo-realistic robot images from rendered robot images. To collect training samples, we use teleoperation to gather a small amount of *play* data, where the robot is teleoperated to move randomly within an empty workspace while recording RGB-D images and

corresponding joint states. This ensures a diverse dataset of robot arm configurations, free from occlusions or distractions.

Notably, these training samples are *platform-specific* but *task-invariant*, meaning they only need to be collected once per robot platform, and the trained ControlNet can be used across all tasks. This also opens up the possibility of directly transforming our in-the-wild demonstrations to other robotic arms without the need to design new exoskeletons that match specific robots.

For training, we use a batch size of 88 and a learning rate of  $10^{-5}$ , while keeping other hyperparameters at their default settings. We use 50 DDPM sampling steps [34] with a guidance scale of 9.0 [35]. The prompt for generating robot images for our robot platform is set to:

*robotic arms, dual arm, industrial robotic manipulator, metallic silver color, mechanical joints, precise mechanical details, gripper end effector, high-quality photo, photorealistic, clear and sharp details*

### E. RISE-2 Implementation

**Data Processing.** The color image is resized to  $448 \times 252$  for DINOv2 backbone [70] and  $640 \times 360$  for ResNet-18 backbone [30]. The depth image is resized to  $640 \times 360$  before creating the point cloud. The camera intrinsics are adjusted accordingly. Both the point clouds and actions are in the camera coordinate system. The point cloud is down-sampled with a voxel size of 5mm. For the data collected with teleoperation, we crop the point clouds using the range of  $x \in [-0.7m, 0.7m]$ ,  $y \in [-0.3m, 0.55m]$  and  $z \in [0.9m, 1.55m]$ . For the data collected with *AirExo-2*, we crop the point clouds using the range of  $x \in [-0.7m, 0.7m]$ ,  $y \in [-0.3m, 0.45m]$  and  $z \in [0.75m, 1.4m]$ .

The robot trajectories are sampled using differences of translation, rotation and gripper width to remove redundant actions. For the action at two adjacent timesteps, if all the differences are less than the thresholds, only the first action is retained. The threshold for translation and gripper width is 5mm and the rotation threshold is  $\pi/24$ .

**Network.** The sparse encoder adopts a ResNet-like architecture built upon MinkowskiEngine [19]. The dense encoder adopts DINOv2-base [70] as the 2D backbone with the output channel of 128. In the spatial aligner, we use  $M = 3$  for feature alignment. The aligned features are fused by shared MLPs with the size of (256, 256, 256), and then fed into another sparse network. The two sparse networks are detailed in Tab. VII. The transformer in action generator contains 4 blocks, in which we set  $d_{\text{model}} = 512$  and  $d_{\text{ff}} = 2048$ . The channel number of the readout token is 512. The diffusion head adopts a CNN implementation [17] with 100 denoising iterations in training and 20 iterations in inference. The output action horizon used in experiments is 20.

**Training.** *RISE-2* is trained on 4 Nvidia A100 GPUs. The batch size is 240, the initial learning rate is  $3e-4$ , and the warmup step is 2000. We employ a cosine scheduler to adjust the learning rate during training. 20% of the color images are augmented using a color jitter with (brightness, contrast, saturation, hue) parameters set to (0.4, 0.4, 0.2, 0.1).

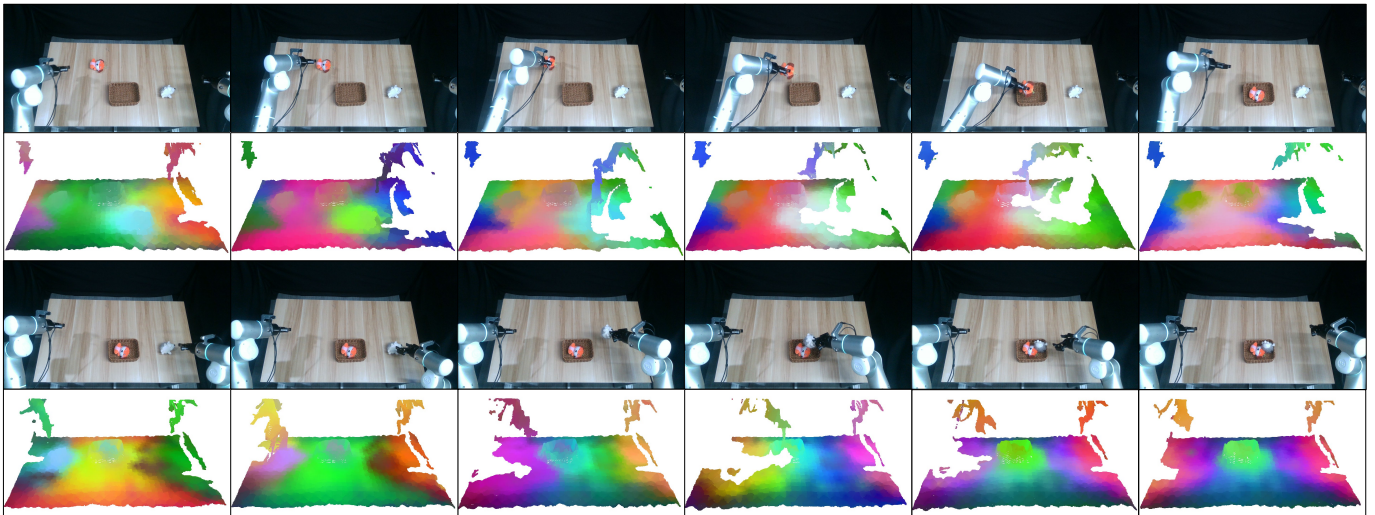


**Fig. 11: Visualization of Sparse Semantic Features.** The colors are obtained by performing PCA on the features. The original sparse semantic features are aligned to the input point cloud using weighted spatial interpolation function in the spatial aligner for clearer visualization.

Layer Name	Sparse Encoder	Spatial Aligner
init_conv	$k = [3, 3, 3]$ , $c = 32$ , $d = 1$ , $s = 1$ 2x mean pooling	-
conv1	$k = [3, 3, 3]$ , $c = 32$ , $d = 1$ , $s = 1$	$k = [3, 3, 3]$ , $c = 256$ , $d = 4$ , $s = 4$
conv2	$k = [3, 3, 3]$ , $c = 64$ , $d = 2$ , $s = 1$	$k = [3, 3, 3]$ , $c = 256$ , $d = 1$ , $s = 2$
conv3	$k = [3, 3, 3]$ , $c = 128$ , $d = 4$ , $s = 1$	$k = [3, 3, 3]$ , $c = 512$ , $d = 1$ , $s = 2$
conv4	$k = [3, 3, 3]$ , $c = 128$ , $d = 8$ , $s = 2$	$k = [3, 3, 3]$ , $c = 512$ , $d = 1$ , $s = 2$
final_conv	$k = [1, 1, 1]$ , $c = 128$ , $d = 1$ , $s = 1$	$k = [1, 1, 1]$ , $c = 512$ , $d = 1$ , $s = 1$

**TABLE VII: Sparse Convolutional Network Parameters of the RISE-2 Policy.** Both sparse encoder and spatial aligner utilize MinkResNet [19] for point cloud encoding.  $k, c, d, s$  stand for the kernel size, output channel number, dilation and stride in the convolutional layers respectively.

### F. Action Representations

We conduct additional experiments on action representations for the *Collect Toys* task, comparing relative and absolute action representations. The results in Tab. VIII show that while relative action representation sometimes yields better results, absolute action representation provides more stable performance, particularly in terms of generalization. Therefore, we use absolute action representations throughout our experiments, except for the case study in §V-B.

### G. Accuracy Analysis

To evaluate action accuracy, we designed a special evaluation board with three tracks, as illustrated in Fig. 12. Each track has fixed holes spaced 2 cm apart. We created custom connectors for both the *AirExo-2* and UMI [18] that fit into

Method	Action Repr.	Success Rate (%) $\uparrow$		
		in-domain	background	object
DP [17]	relative	37.5	<b>20.0</b>	<b>5.0</b>
	absolute	<b>40.0</b>	12.5	<b>5.0</b>
CAGE [105]	relative	<b>72.5</b>	32.5	35.0
	absolute	65.0	<b>45.0</b>	<b>42.5</b>

**TABLE VIII: Evaluation Results of Different Action Representations on the Collect Toys Task.** Absolute action representation leads to a more stable performance.

these fixed holes, allowing us to collect position data. By sequentially placing the connectors into each fixed hole along the track, we can calculate the relative movement distance between two adjacent fixed holes and compare it with the true value (20 mm) to calculate the error.

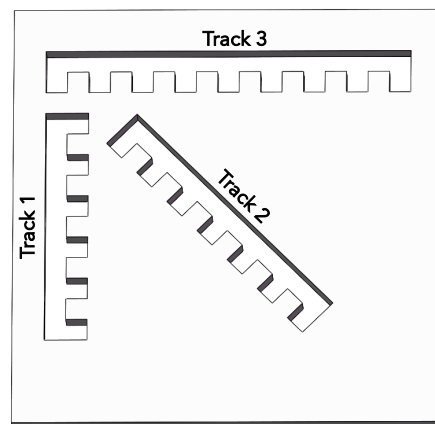


**Fig. 12: The Designed Evaluation Board for Accuracy Analysis.**

#### *H. Visualization of Sparse Semantic Features*

Fig. 11 visualizes the sparse semantic features obtained from the dense encoder by projecting the 2D feature map to 3D form using the reference coordinates. The sparse semantic features are aligned to the input point cloud using weighted spatial interpolation detailed in §IV-B.

Although the 2D feature map output by the dense encoder is in low resolution ( $32 \times 18$ ), we still observe clear and distinguishable continuous feature variations on the aligned features, where the targets at the current step can be easily identified from the entire scene. Such characteristic ensures precise feature fusion in the spatial domain. Additionally, we find that the features from DINOv2 change significantly as the task progresses, enabling the model to clearly understand the global state at the current time.